SANDIA REPORT

SAND2015-8329
Unlimited Release
Printed Month and Year

Organosilicon-Based Electrolytes for Long-Life Lithium Primary Batteries

Kyle R. Fenton, Ganesan Nagasubramanian, Chad L. Staiger, Harry D. Pratt III, Susan B. Rempe, Kevin Leung, Mangesh I. Chaudhari, Travis M. Anderson

Prepared by
Sandia National Laboratories
Albuquerque, New Mexico 87185 and Livermore, California 94550

Sandia National Laboratories is a multi-program laboratory managed and operated by Sandia Corporation, a wholly owned subsidiary of Lockheed Martin Corporation, for the U.S. Department of Energy's National Nuclear Security Administration under contract DE-AC04-94AL85000.

Issued by Sandia National Laboratories, operated for the United States Department of Energy by Sandia Corporation.

Available to DOE and DOE contractors from
U.S. Department of Energy
Office of Scientific and Technical Information
P.O. Box 62
Oak Ridge, TN 37831

Telephone: (865) 576-8401
Facsimile: (865) 576-5728
E-Mail: reports@osti.gov
Online ordering: http://www.osti.gov/scitech

Available to the public from
U.S. Department of Commerce
National Technical Information Service
5301 Shawnee Rd
Alexandria, VA 22312

Telephone: (800) 553-6847
Facsimile: (703) 605-6900
E-Mail: orders@ntis.gov
Online order: http://www.ntis.gov/search

SAND2015-8329
Unlimited Release
Printed Month Year

Organosilicon-Based Electrolytes for Long-Life Lithium Primary Batteries

Kyle R. Fenton[1], Ganesan Nagasubramanian[1], Chad L. Staiger[2], Harry D. Pratt III[3], Susan B. Rempe[4], Kevin Leung[5], Mangesh I. Chaudhari[4], Travis M. Anderson[3]

[1]Power Sources Design and Development
[2]Materials, Devices, and Energy Technologies
[3]Power Sources Research and Development
[4]Biofuels and Biomaterials Science and Technology
[5]Radiation, Nanomaterials, and Interface Science

Sandia National Laboratories
P.O. Box 5800
Albuquerque, New Mexico 87185-MS0614

Abstract

This report describes advances in electrolytes for lithium primary battery systems. Electrolytes were synthesized that utilize organosilane materials that include anion binding agent functionality. Numerous materials were synthesized and tested in lithium carbon monofluoride battery systems for conductivity, impedance, and capacity. Resulting electrolytes were shown to be completely non-flammable and showed promise as co-solvents for electrolyte systems, due to low dielectric strength.

ACKNOWLEDGMENTS

This work was supported by the Sandia Laboratory Directed Research and Development (LDRD) program. Authors gratefully acknowledge technical contributions to this work by Todd Monson, Lorie E. Davis, Jill L. Langendorf, Mark Rodriguez, Todd Monson, and Scott Spangler. Authors gratefully acknowledge technical discussions with Stephen Harris, Christopher J. Orendorff, and Zonghai Chen. Collaboration with Xinli You and Lawrence Pratt at Tulane University are gratefully acknowledged by Mangesh I. Chaudhari and Susan B. Rempe. We would also like to acknowledge Perla Balbuena, Texas A&M University, and the funding for that collaboration through the Department of Energy, Office of Vehicle Technologies Battery Materials Research Program.

CONTENTS

FIGURES

TABLES

NOMENCLATURE

Å	Angstrom (10^{-10} meters)
ABA	Anion binding agent
Bn	Benzyl
CF_x	Carbon monofluoride
CV	Cyclic voltammetry
DEC	Diethyl carbonate
DMC	Dimethyl carbonate
DMMP	Dimethyl methylphosphonate
EC	Ethylene carbonate
EIS	Electrochemical impedance spectroscopy
EMC	Ethyl methyl carbonate
F-EC	Fluoroethylene carbonate
OAc	Acetate
OMe	Methoxy
M_n	Number average molecular weight
NMR	Nuclear magnetic resonance
PDMS	Poly(dimethylsiloxane)
PhH	Benzene
PhMe	Toluene
PEG	Poly(ethylene glycol)
PPTS	Pyridinium *p*-toluenesulfonate
Pt[dvs]	Karstedt's catalyst, platinum(0)-1,3-divinyl-1,1,3,3-tetramethyldisiloxane
THF	Tetrahydrofuran
TMS	Trimethylsilyl

1. INTRODUCTION

We aim to develop new lithium primary power sources designed to have wider operating temperatures using inherently safe materials to increase the performance and safety of power sources used in multiple testing applications. The Achilles' heel of organic electrolytes used in Li primary and secondary batteries is their instability at elevated temperatures and safety concerns including fire and explosion. In order to eliminate flammability concerns at elevated temperatures, we propose to develop a new class of 'organosilicon' electrolyte materials that have high temperature stability, high ionic conductivity, are nonflammable, nontoxic, and have low viscosities (~1.4 cP). Informed by new DFT models, these compounds will offer high temperature (>75 °C) and low temperature (-40 °C) performance in a nontoxic, nonflammable electrolyte solvent. We will fabricate CF_x (carbon monofluoride)-based Li-Primary cells with these optimized electrolytes, employing advanced packaging concepts and focusing on needs for safe, high energy density primary batteries applications.

Many current systems employ lithium primary batteries due to their high energy densities and wide operational temperature range. However, many of the currently employed systems become lack-luster when evaluating either chemical safety or electrochemical utilization of the cathode material. Figure 1 shows a comparison between several different commonly used battery systems

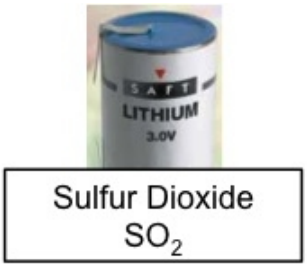

Sulfur Dioxide
SO_2

- Theoretical Energy Density: 1110 Wh/kg
- Useable Energy Density: 300 Wh/kg and 500 Wh/L
- ~ 30 % utilization
- Temperature: -55C to 70C
- Liquid cathode system
- Safety concerns:
- Toxic and can product LiCN via ACN reaction

Thionyl Chloride
$SOCl_2$

- Theoretical Energy Density: 1490 Wh/kg
- Useable Energy Density: 510 Wh/kg and 1020 Wh/L
- ~35 % utilization
- Temperature: -55C to 150C
- Liquid cathode system
- Safety concerns:
- Gas generation and toxic, limits high rates

Carbon Monofluoride
CF_x

- Theoretical Energy Density: 2260 Wh/kg
- Useable Energy Density: 290 Wh/kg and 510 Wh/L
- ~10% utilization
- Temperature: -20C to 85C
- Solid Cathode – allows for drastic changes
- Previous SNL builds as high as ~300 Wh/kg
- Limited safety concerns – safe primary chemistry

Figure 1. Comparison of currently utilized lithium primary batteries.

It should be noted that many of the lithium carbon monofluoride (CF_x) systems that are currently employed do not currently utilize the entirety of the available capacity with that electrochemical couple. Interestingly, that implies that the lithium primary system with the most available room for increased utilization is the CF_x cathode system. Since the carbon monofluoride system is a solid cathode (unlike the SO_2 or $SOCl_2$), the performance increase resides solely in the electrolyte.

Organosilicon electrolytes exhibit several important properties for use in lithium cells that include: 1) high conductivity/low viscosity and 2) thermal/electrochemical stability. The systematic manipulation of the silicon oxide backbone geometry and repeat unit length as well as the appended ethylene oxide moieties allows for fine-tuning of the thermal and electrochemical properties of the electrolyte. These manipulations also allow for incorporation of innovative functionalities such as anion binding agents (ABAs), which dramatically change the electrochemical properties of the electrolyte and bind the fluoride anion (a byproduct of discharge) leaving lithium ions available for incorporation into the electrolyte. This work will enable the design of unique multifunctional, thermally stable organosilicon compounds with a wide variety of tunable properties. The knowledge developed in this program is expected to have an immediate impact on battery technology, but is more broadly relevant to other applications, which range from semiconductor manufacturing materials to drug delivery agents where organosilicon is being investigated.

The primary goal for this program is to develop a new class of silicon based electrolytes, which are thermally stable and can be tailored for application specific needs. These multifunctional electrolytes will be synthesized, characterized, evaluated for thermal and electrochemical performance, and optimized for use in large format (several Ah 18650 and prismatic) cells.

In this work, there are three technical tasks we will focus on, which will expedite our efforts towards development of new power sources. The three areas are interdependent in that they form a loop where the observation from one area is cyclically fed into the other with an end focus to produce a robust product. For example, the data on electrolyte will be fed into the modeling effort to fine tune its predictions, which in turn will be fed into the electrolyte area to further improve the electrolyte properties.

<u>Organosilicon electrolyte synthesis and characterization:</u>
Current state-of-the-art efforts to develop organosilicon electrolytes focus on their use in lithium-ion applications. These efforts have demonstrated many positive characteristics for these materials such as being nonvolatile, nonflammable, oxidatively resistant, and nontoxic [1]. These properties may be finely tailored through control of geometry (comb, double-comb, cyclic, network, or linear structure), through variation in chain lengths (typically 3–7 repeat units), and through careful selection of appended ABAs. The flexible siloxane backbone facilitates low energy bond rotations that impart wide temperature stability and low viscosity allowing for wide temperature operation while their conjugated polyethylene oxide (PEO) units solvate lithium cations via complexation with oxygen. These materials have been demonstrated to have conductivities up to ~10^{-3} S cm^{-1} when doped with a lithium salt [2]. Although these compounds display excellent lithium solvation, they have poor lithium mobility due to strong ion pairing with its conjugate anion. Attempts to alleviate this problem with the introduction of polar

carbonate groups have been met with limited success because the increased dielectric constant is offset by higher viscosity [3]. We propose a transformational approach to this problem by utilizing an anion-binding agent (ABA). These ABA molecules dissociate LiF by binding the fluoride ion, allowing for use of the stable LiF salt in lithium batteries [4,5]. We will conjugate an ABA to the siloxane/silane backbone to create a bi-functional electrolyte, as depicted in Figure 2 for the linear version of the electrolyte. The bi-functionality of the proposed electrolyte is due to the PEO moieties to solvate lithium (control of ionic conductivity within the electrolyte) and ABA groups to bind the fluoride anion and thus facilitate lithium fluoride dissolution (effectively preserving the porous structure of the cathode). This unique ability to control both the electrolyte conductivity (by control of the siloxane geometry and repeat chain length) and electrode morphology/properties simultaneously gives potential to greatly revolutionize lithium electrolyte understanding and operation.

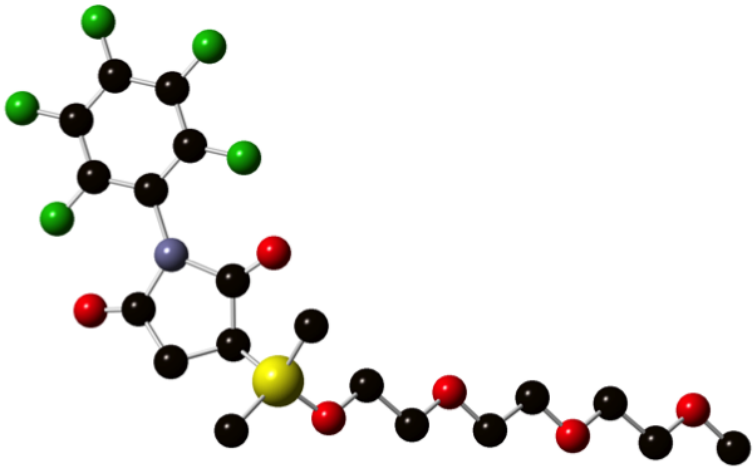

Figure 2. Rendering of proposed linear bifunctional electrolyte for simultaneous control of electrode and electrolyte conductivity in a lithium primary cell.

Additionally, the use of this type of multifunctional electrolyte is ideal in the case of the CF_x lithium primary battery system. This is due to the discharge mechanism for the carbon monofluoride battery as seen in Figure 3.

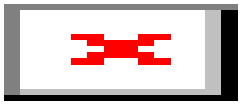

Figure 3. Discharge reactions for the lithium carbon monofluoride battery system.

Development of an electrolyte system that is capable of both supporting battery discharge and dissolution of lithium fluoride will aid in the performance in the CF_x system. The primary mechanism for loss of capacity is the development of lithium fluoride salts, which effectively block transport within the cathode. An electrolyte capable of both supporting conductivity and

transport while simultaneously clearing the pore of discharge products could potentially increase the total system utilization of the carbon monofluoride battery chemistry.

Fabrication and evaluation of organosilicon containing CF_x primary batteries:
We plan on evaluating each of the organosilicon electrolytes using the $LiCF_x$ primary lithium battery system. This decision is based on the high practical energy density of this chemistry (~1100 Wh/L), long shelf life, and the ability for this chemistry to have radical changes based upon electrolyte changes. The currently used $LiSOCl_2$ or $LiSO_2$ cells for many applications have potential safety issues associated with their operation. Furthermore, recent changes in the occupational exposure limits for SO_2 gas are at or below the current detection limits (5 ppm) for current sensors, posing a dangerous situation for those involved in testing here at Sandia and for many of our customers. In preparation for future power needs and safety considerations, we believe that the CF_x system in combination with new electrolytes will be able to provide the safety and necessary energy. During this program, we will evaluate and optimize a standard $LiCF_x$ electrode in order to evaluate the changes in organosilicon materials and their effect on temperature performance, rate capability, and transient behavior during discharge, and safety response. Selection and understanding of battery materials is necessary as it provides the basis for evaluation of the organosilicon electrolytes. Many factors such as fluorination level, binder selection, conductive additive selection, and electrochemical parameters affect cell performance and will be controlled rigorously. During the initial stages of the program, evaluations will take place on the scale of small pouch cells and coin cells. We aim to develop a fully characterized high-energy power source by the end of the program, which employs the developed bifunctional or multifunctional organosilicon electrolyte. These cells will be fabricated and characterized in both 18650 and prismatic cells formats, as seen in Figure 4.

The bi-functionality that is possible with organosilicon electrolytes using ABA ligands has potential to greatly increase the performance of lithium CF_x batteries. Lithium CF_x discharge products are LiF and C, which gives rise to increased electrical conductivity of the cathode due to the increased carbon loading. The LiF salt causes dramatic changes to the transport properties within the cell due to pore clogging and electrode fouling. Inclusion of an ABA ligand to the organosilicon electrolyte allows for dissolution of the LiF salt directly, which not only increases the lithium ion concentration in the electrolyte (increased ionic conductivity) but also prevents the fouling of the electrode and effectively increases the carbon loading in the electrode (increased electronic conductivity). This also leads to potential to build batteries having low salt loading (higher stability and longer shelf life) for the initial battery start up that effectively scavenge highly stable lithium fluoride salt during discharge yielding high performing and safer cells [6,7]. Inclusion of other agents for specific purposes, would allow for development of multifunctional electrolytes. The effectiveness of this radical concept for controlling battery performance will be rigorously evaluated, as there is very little precedence for a system such as the proposed.

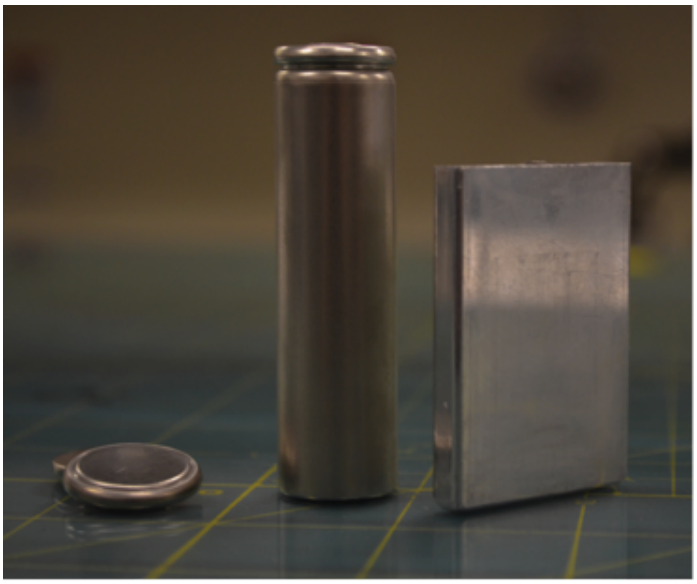

Figure 4. Cell test platforms planned for program. From left to right: 2032 coin cell tests, 18650 large format tests, and custom sized prismatic cells (application specific).

Research Area 3 – Molecular modeling of electrolyte and cell performance:
A combination of electronic structure based on density functional theory (DFT) and classical force field (CFF) molecular dynamics (MD) simulations will be used to model viscosity, dielectric properties, salt solvation (diffusion properties), and other critical electrolyte parameters as a function of solvent molecule architecture and temperature. In the first year we will parameterize CFF using DFT predictions and perform/refine MD simulations for solvent molecules that have been synthesized and examined experimentally. We will confirm that modeling predictions reproduce the correct trends and produce reasonable quantitative values for viscosity and other properties as a function of temperatures. In outlying years, we will perform "computational materials design," modify the solvent structure (e.g., by lengthening the size of the hydrocarbon groups), predict the metric of success of the most promising solvent molecule and use such predictions to guide and inform the optimal solvent molecules to be synthesized and applied in battery environments.

Discharge products for several of the commonly used primary battery chemistries, including $SOCl_2$, are currently classified as hazardous materials with low exposure limits [8,9]. The exposure limits for these materials vary, but are generally in the single ppm range. This excludes them for use in many applications, particularly when operator safety and proximity is a key consideration. This has inspired a renewed focus in development and exploration of other lithium primary batteries to substitute for those having chemical safety concerns. Demand for batteries with long life, lightweight, high energy density, and eco-friendly features are driving growth in identifying alternative chemistries. For our internal applications, the alternative chemistries should: 1) have long life and high capacity, 2) produce non-toxic discharge products, 3) perform over a wide temperature range, and 4) be composed of thermally stable materials.

Lithium carbon monofluoride ($LiCF_x$) chemistry satisfies the first two criteria. However, like any other lithium chemistry, it is also stymied by solvent flammability problems and low temperature performance problems due to the fouling of the cathode pores by the discharge product. Improving these problems is central to the adoption of this chemistry. To overcome the two problems we are proposing to use a nonflammable solvent in conjunction with a thermally stable salt. By adding neutral anion binding agents (ABA) capable of dissolving the discharge product, which in this case is lithium fluoride (LiF), to this safe electrolyte, cathode fouling during discharge may be mitigated. Addition of sub-stoichiometric amounts of LiF to the electrolyte containing excess amount of ABA dissolved allows the solution to contain free Li^+ABAF^- salt complex and sufficient free non-complexed ABA for dissolving the discharge product. The principal goal of this approach is to show that cell performance can be enhanced by dissolving the discharge product in real time. This idea has far reaching impact beyond Li-CF_x in improving battery performance of, for example, rechargeable batteries like Li-O_2 and Li-ion batteries with conversion compounds that have potentially huge stored energy but suffer from voltage hysteresis and poor recharge capability [9]. The down side to this implementation is that the charge voltage can potentially be a lot higher than the discharge voltage, which amounts to expending more energy to recharge the battery. If an ABA can be identified that can dissolve the discharge product, for example Li_2O_2 then reversibility and performance of the Li-O_2 battery can be vastly improved [10-12]. The same rationale is applicable for the conversion chemistry.

Parts of this work focus on evaluating DMMP solvents in conjunction with tris(pentafluorophenyl) borane (TPFB) bound to LiF, which is supplementary to previous efforts to understand ABA performance in nonflammable solvents [13-15]. DMMP has been studied extensively as a fire retardant in Li-ion cells [16-19]. Pairing DMMP with TPFB-LiF synergistically endows the cell chemistry with both enhanced thermal stability and improved electrochemical performance.

The propensity of the ABA to dissolve LiF has been taken advantage of for improving Li-ion cell performance before. For example McBreen proposed the use of ABAs, also known as anion receptors, to dissolve the accumulated LiF, due to the decomposition of the $LiPF_6$ salt, on cathode surface in Li-ion batteries [20]. They demonstrated that the cathode can be rejuvenated by dissolving the LiF layer. West [21] *et.al. h*ave demonstrated reversible intercalation of F^- in graphite from an organic solution containing an ABA and LiF. However, our work focuses on dissolving the generated LiF in the Li-CFx discharge to improve the ohmic and interfacial resistances as the cell discharge. We are accomplishing these by varying the composition of the ABA-LiF complex salt in the electrolyte. In this paper we will discuss the thermal and the electrical properties of the DMMP/ABA-LiF electrolyte and the electrical performance of CFx materials obtained from different vendors in the above electrolyte.

2. SYNTHESIS AND MATERIALS DEVELOPMENT

2.1. Siloxane-Glycol Electrolyte Solvent

A series of siloxane-glycol electrolyte solvents were prepared to assess the impact of the siloxane and ethylene glycol repeat units on battery performance. Two different synthetic routes were utilized to allow variation of the siloxane and ethylene glycol repeat units. The synthesis of a monosilane with varied ethylene glycol repeat units is shown in Figure 5 [22]. Commercially available ethylene glycol monomethyl ethers (n = 3 or 5) **1** were deprotonated with triethylamine in tetrahydrofuran and subsequently reacted with chlorotrimethylsilane to give silyated glycol ether **2** in high yield. The silylated glycol ether was further purified by fractional distillation.

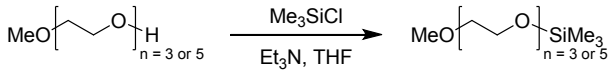

1 **2**

Figure 5. Preparation of glycol-monosilane electrolyte solvents.

To increase the number of repeat units in the siloxane from one to three, a two-step procedure was utilized (Figure 6) [23]. The commercially available ethylene glycol monomethyl ethers (n = 3 or 5) were initially deprotonated with sodium hydride in tetrahydrofuran and subsequently reacted with allyl bromide to yield allylated ether **3**. Allylated ether **3** was then hydrosilylated with 1,1,1,3,3,5,5-heptamethyltrisiloxane using Karstedt′s catalyst to yield glycol-trisiloxane **4**. Glycol-trisiloxane **4** was further purified by fractional distillation.

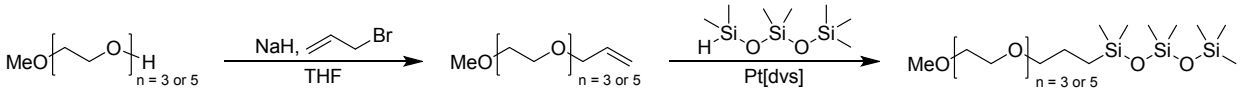

1 **3** **4**

Figure 6. Preparation of glycol-trisiloxane electrolytes.

With the preparation of small molecule siloxane-ethylene glycol electrolyte solvents, a polymeric comb structure was also prepared. The synthesis of this material is similar to the preparation of trisiloxane compounds **4** in Figure 6. Briefly, polymethylhydrosiloxane **5** (M_n = 1700 to 3200) was reacted with allylated ether **3** (n = 3) in the presence of Karstedt′s catalyst to yield comb polymer **6** (Scheme 3). A number of different purification strategies including activated charcoal, SiO_2 chromatography and distillation, were performed on polymer **6**, but the color post-purification was slightly yellow, suggesting Pt removal was incomplete. Ultimately the high viscosity of this polymer may limit its utility in a battery.

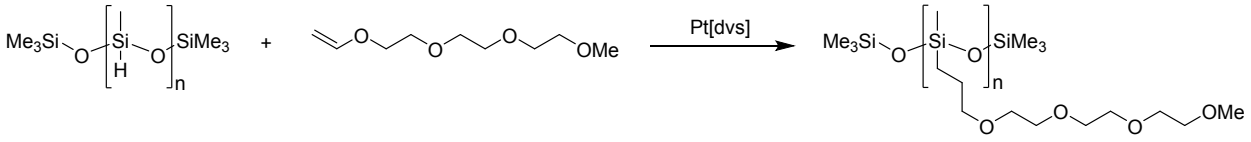

5 **3** **6**

Figure 7. Preparation of a siloxane-glycol comb polymer.

2.2. Boron Based Anion Binding Agents (ABAs)

2.2.1. Attachment of electrolyte solvent through fluorinated phenyl group

Several synthetic routes were attempted to prepare a compound containing both the electrolyte (glycol and siloxane) and ABA functionality. Siloxane-ethylene glycol-ABA **11** was initially targeted (Figure 8). Previous studies found the electron withdrawing oxaloto group enhanced F-binding and favorable battery electrochemistry, so we wished to maintain that functionality within ABA **11**. A nucleophilic aromatic substitution on bromopentafluorobenzene with deprotonated vinyl ether **7** yielded fluorinated ether **9** [24]. Fluorinated ether **9** was then hydrosilyated with heptamethyltrisiloxane using Karstedt′s catalyst to give aryl bromide **10** [25].

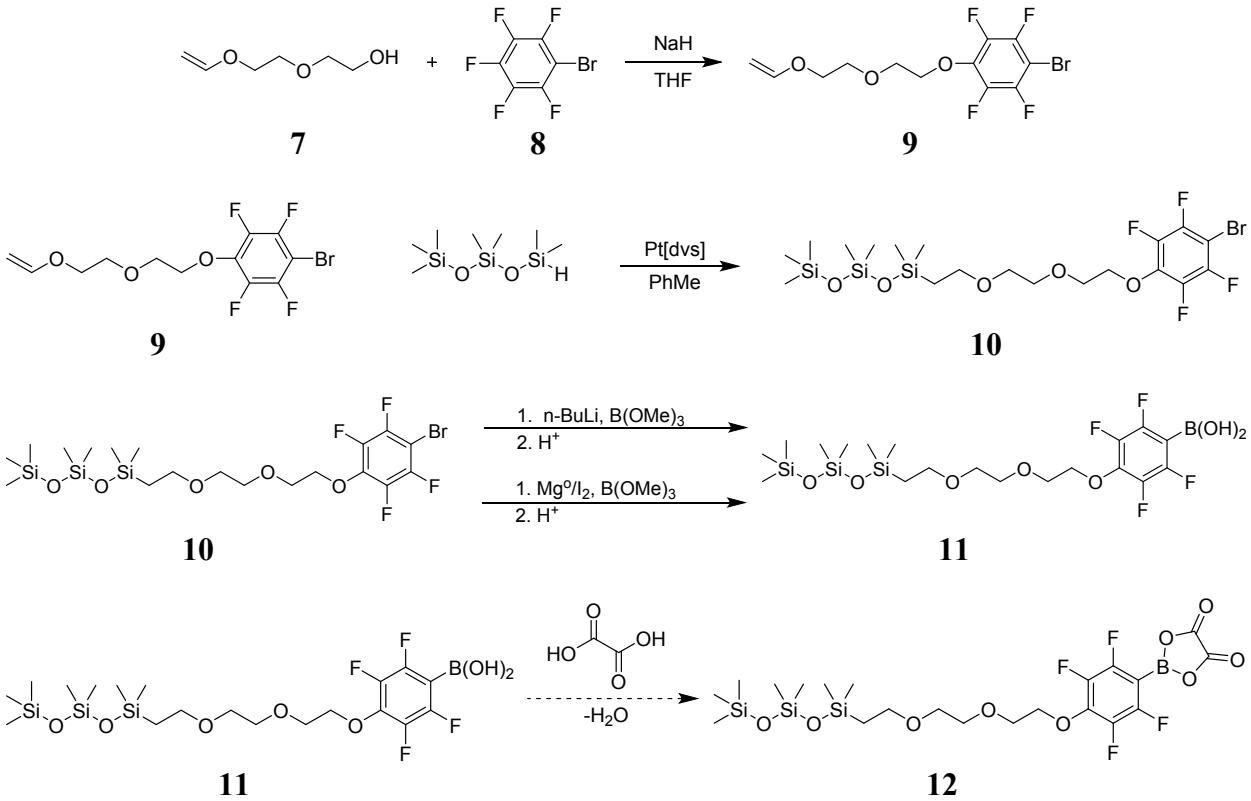

Figure 8. Synthetic route to siloxane-glycol ABA 12.

Two different methods were attempted to attach boron functionality to the aryl group (Figure 8) [26]. First, lithium-halogen exchange followed by the addition of trimethyl borate and subsequent acidic work-up should have yielded boronic acid **11**. However, ^{1}H NMR showed the siloxane functionality did not survive the reaction and/or work up conditions. Also ^{11}B NMR showed boric acid, $B(OH)_3$, as a product and that no boron functionality was attached to the aryl group. Attempts to isolate the dimethyl ester (i.e., no acidic workup) were also unsuccessful.

The second method to attach the boronic acid functionality was through the use of a Grignard reaction. Aryl bromide **10** was reacted with magnesium turnings and subsequently added to trimethyl borate. Starting material was typically recovered indicating the Grignard reagent never formed.

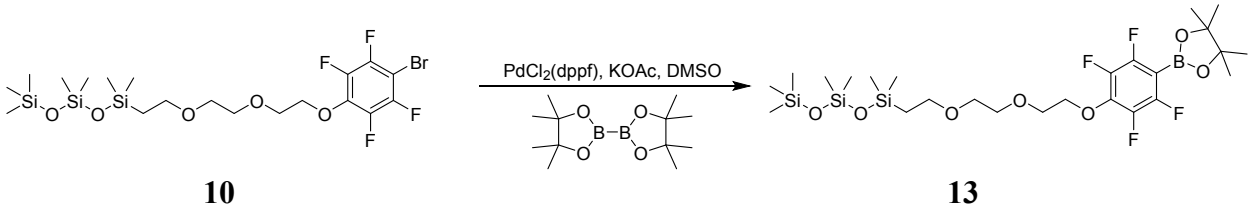

10 **13**

Figure 9. Preparation of a siloxane-glycol ABA 13.

Since the route to install boronic acid functionality was unsuccessful, an alternative method to directly prepare a pincol functionalized boronate was investigated [27]. Palladium catalyzed cross coupling[1] of bis(pinacolato)diboron with aryl bromide **10** yielded pinacol boronate **13**. ^{19}F and ^{11}B NMR showed that the pinacolato boron group did substitute at the bromide, however purification of this compound for use in electrochemical studies proved difficult. Extractive workups, distillation and SiO_2 chromatography were all tried to increase the purity of pinacol boronate **13,** but were unsuccessful.

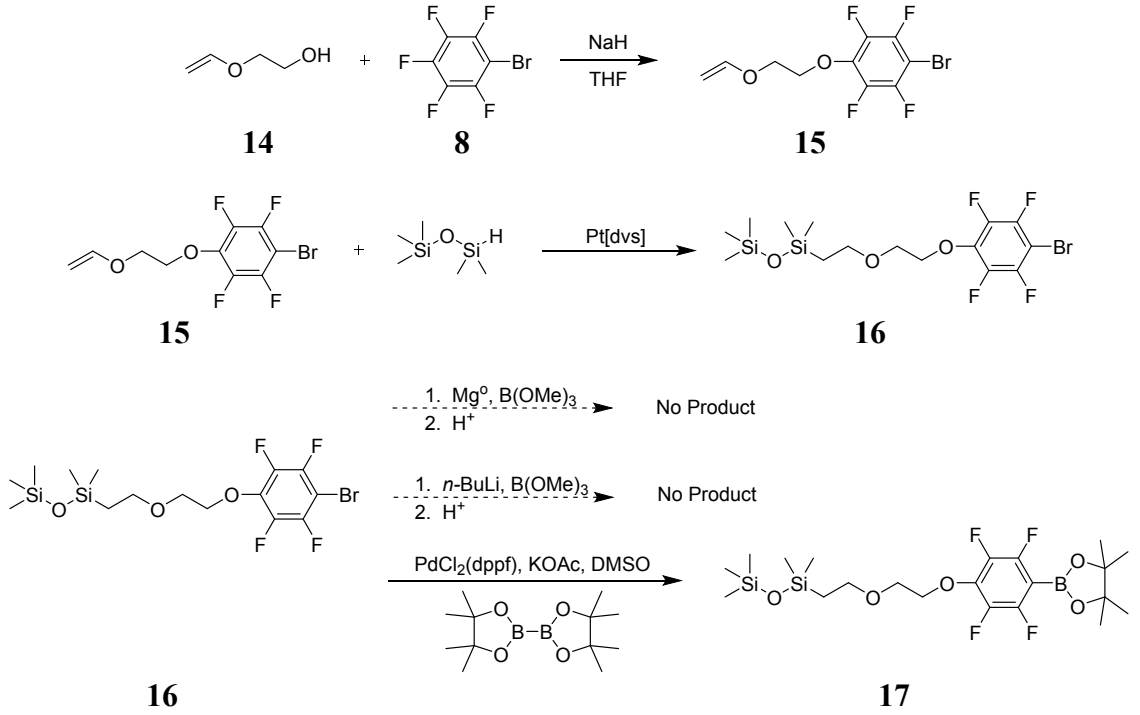

14 **8** **15**

15 **16**

16 **17**

Figure 10. Preparation of a siloxane-glycol ABA 17.

Given the high molecular weight and viscosity of boronate **13**, a version with less glycol and siloxane repeat units was prepared in the hopes of decreasing viscosity and making purification easier (Figure 10). The preparation of aryl bromide **16**, similar to that of bromide **10** and

allowed for a more pure compound going into the boronation reactions. However the lithium-halogen and Grignard reactions did not yield any boronic acid product. The Pd catalyzed cross coupling was successful to give ABA **17**, but as with its high molecular weight analog, obtaining a purity sufficient for use in electrochemical studies was not achievable.

An "atom efficient" silane-glycol ABA synthesis was also attempted (Figure 11). The target compound contained one glycol, no siloxane linkages and the hydrocarbon spacer between the silicon and glycol was eliminated. The lower molecular weight of this molecule could permit vacuum distillation of ABA **21**. However, the lability of the Si-O bond in ABA **21** interfered with all of the boronation reactions.

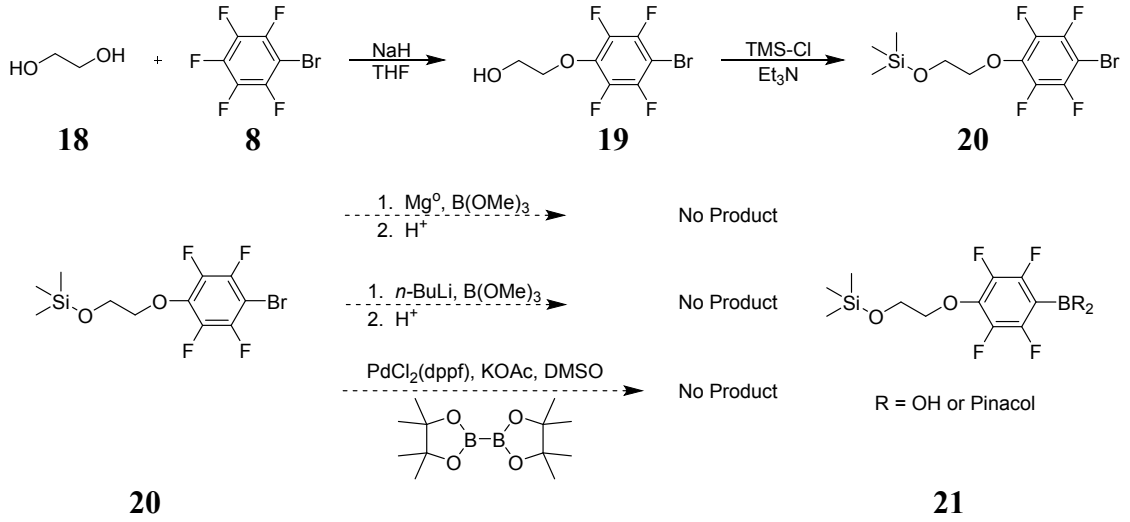

Figure 11. Attempted preparation of a silane-glycol ABA 21.

2.2.2. Attachment of electrolyte solvent through dioxo- functionality

The difficulty associated with the boronation reaction in the previous section necessitated an adjustment in the synthesis methodology. Another concept explored was incorporating the siloxane-glycol functionality through the boronic ester, rather than through the fluoroaromatic. A benefit of this strategy is the ease of synthesis, however unacceptable anion binding performance at the boron center may become an issue due to replacement with less electron withdrawing moieties (e.g., oxalate versus glycol).

A number of small molecules were prepared to evaluate the methodology. Each diol in Figure 12 was separately reacted with pentafluorophenylboronic acid (**22**) in refluxing toluene [28]. A Dean-Stark apparatus was used to continuously remove water from the reaction flask. All dioxaborolanes were prepared in high yield and purity. Each compound could be further purified using sublimation (dioxaborolanes **23** and **24**) or vacuum distillation (dioxaborolane **25**).

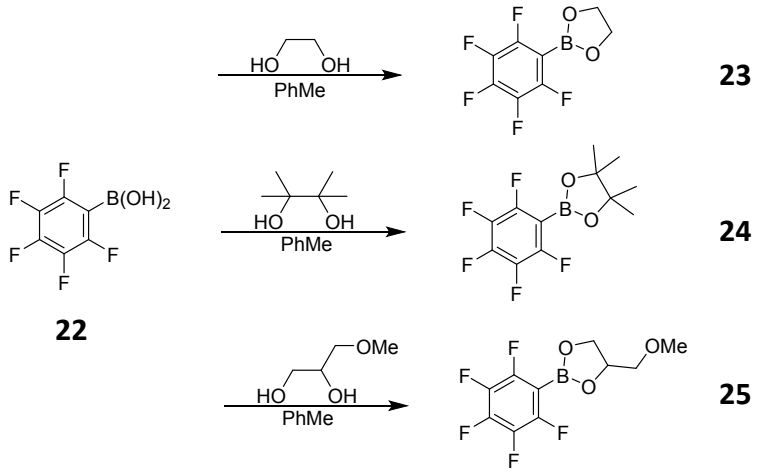

Figure 12. Preparation of a diol ABAs.

To increase the electron withdrawing around the boron center, several test reactions were performed with acetic and glycolic acid (Figure 13). Reaction of pentafluorophenylboronic acid with two equivalents of acetic acid did not yield the desired product (**26**). NMR suggests the pentafluorophenylboronic acid underwent a protodeboronation reaction to give pentafluorobenzene. Modification of the solvent and temperature conditions did not suppress this undesired reaction. Likewise the reaction of glycolic acid did not yield any of boronate ester **27** (Figure 13).

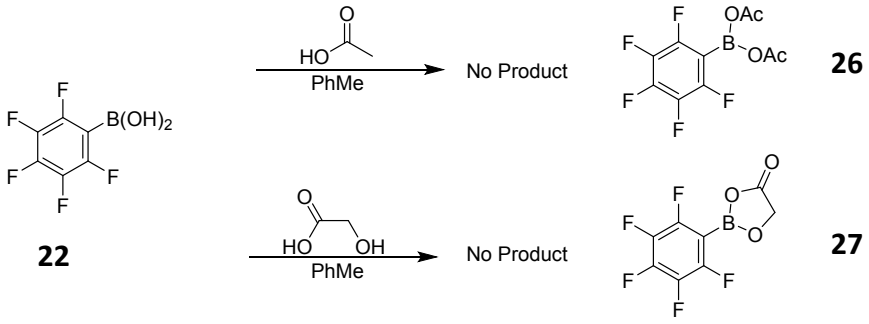

Figure 13. Preparation of carboxylic acid ABAs.

Based on the small molecule syntheses with the diols and acids, a diol with glycol and siloxane functionality was prepared for reaction with pentafluorophenylboronic acid (Figure 14). The diol of allylated glycerol (**28**) was protected as the acetonide by reaction of 2,2-dimethoxypropane and pyridinium *p*-toluenesulfonate (PPTS) in CH_2Cl_2. Hydrosilyation of acetonide **29** with pentamethyldisiloxane and Karstedt's catalyst yielded disiloxane **30**. The acetonide in disiloxane **26** was removed using aqueous HCl in THF to give diol **31**. The yield of the deprotection was quite low (~20 to 30%) relative to the two previous steps and required SiO_2 chromatography prior to the boronation step. NMR suggested the siloxane was partially decomposing during the deprotection. Alternative deprotection reactions were examined including Dowex/H_2O, aqueous acetic acid and iodine/methanol, but yields could not be increased. Refluxing diol **31** in toluene with pentafluorophenylboronic acid lead to a mixture of products that were difficult to purify. Alternatively, diol **31** was reacted with the

pentafluorophenylboronic acid at room temperature in the presence of activated 4 Å molecular sieves. The milder reaction conditions yielded boronic ester **32** as a viscous oil.

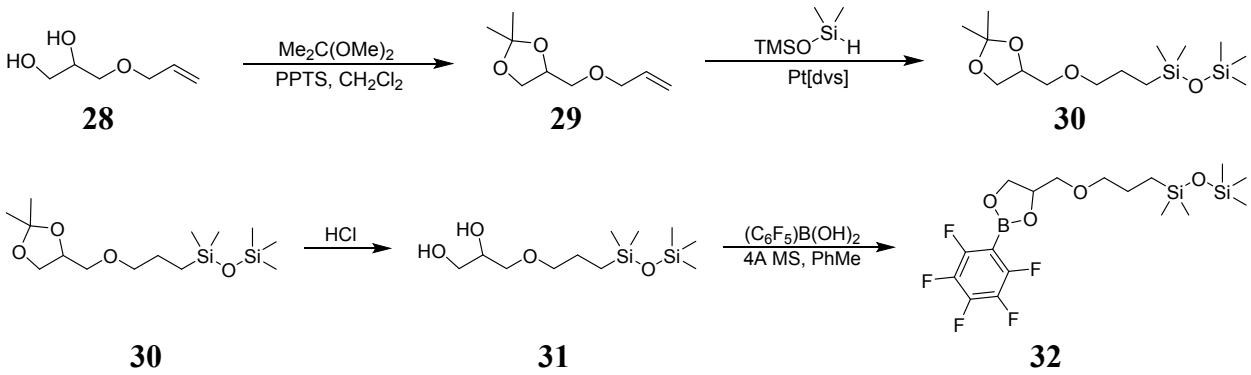

Figure 14. Preparation of ABA 32.

With the success of the boronic ester **32** synthesis an analog was also prepared whereby the siloxane functionality was replaced with a fluorous group (Figure 15). To prepare boronate ester **36**, trifluoroethanol was reacted with (±)-glycidol in the presence of benzyltrimethylammonium hydroxide catalyst to give fluorous diol **35**. Using a Dean-Stark apparatus fluorous diol **35** was refluxed with pentafluorophenylboronic acid in toluene. After concentrating the solution, fluorous boronic ester **36** was purified by vacuum distillation to give a viscous oil.

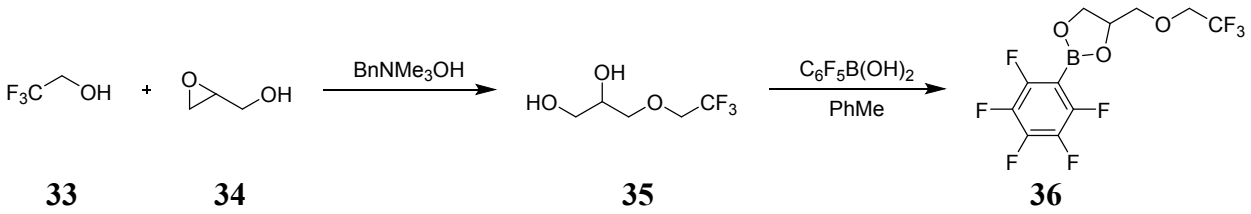

Figure 15. Preparation of fluorous ABA 31.

2.2.3. Anion binding agents with silane/siloxane functionality

The previous section focused placement of the glycol moiety between the ABA center and siloxane functionality. An alternative arrangement to this is to place the siloxane functionality between the glycol and the ABA. In this arrangement, the siloxane is slightly more electron withdrawing to the ABA than a glycol moiety.

A small subset of compounds was targeted to assess the potential of attaching a siloxane to the boron based ABA. Several attempts were made to prepare a trimethylsilyl (TMS) substituted ABA **37** (Figure 16). All of the attempts involved reacting pentafluorophenylboronic acid (**22**) with reagents typically used for silylating alcohol groups [29]. However, formation of silyl substituted ABA **37** was not observed by NMR.

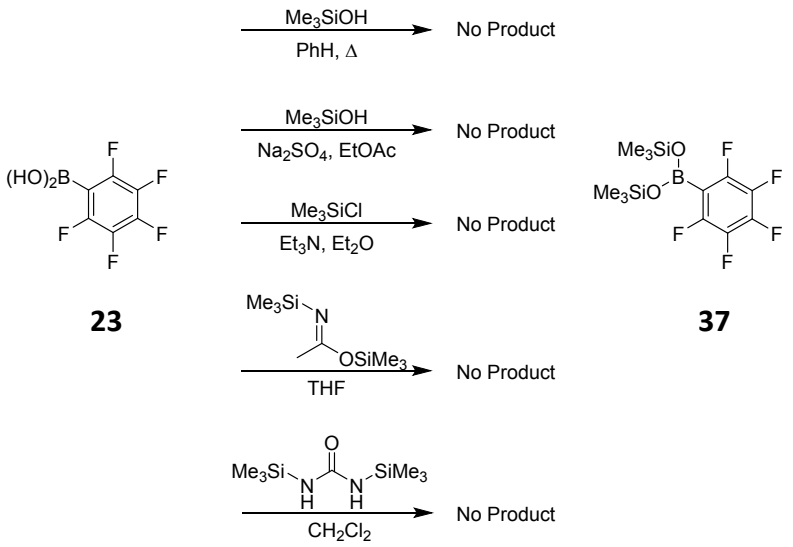

Figure 16. Attempted preparation of trimethylsilyl ABA 31.

Attempts were also made to react dichlorosiloxane **34** with pentafluorophenylboronic acid (**22**) to give *cyclo*-borasiloxane **39**. While the non-fluorinated analog of *cyclo*-borasiloxane **39** are known, the fluorinated analogs have not been previously prepared [30]. Different reaction conditions failed to yield any of *cyclo*-borasiloxane **39**.

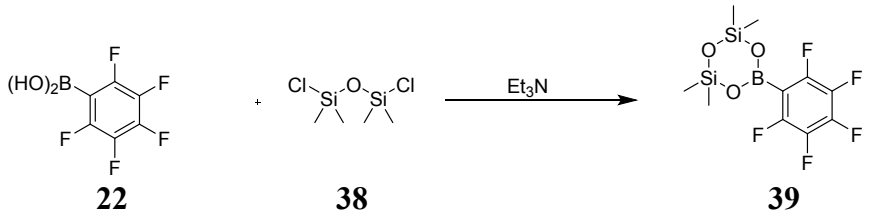

Figure 17. Attempted preparation of *cyclo*-borasiloxane 39.

3. TESTING AND PROTOTYPING

3.1. Identification and evaluation of cathode materials

A survey was conducted to identify potential commercially available materials. Many materials were omitted due to their availability and annual throughput. To be commercially viable as an alternative to many of our battery applications, it was decided that the smaller research type materials companies would be excluded from testing. This led to the identification of approximately three main material suppliers. During the course of this research, one of these suppliers went out of business, which will have consequences in the availability of the materials used.

Materials were purchased and used as received after a preventative bake out at 110 °C under vacuum for 12 hours. This is the standard preparatory process for all battery materials in our laboratory. Materials were processed into slurry (vita infra) and coated on either a manual doctor blade using an elcometer or processed on a reel-to-reel reverse comma coater (see Figure 18).

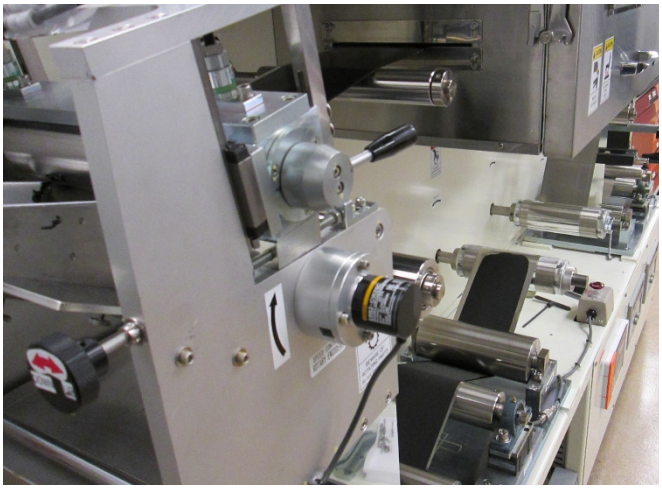

Figure 18. Continuous coating process utilizing a reverse comma coater for the fabrication of lithium CF_x cathode materials.

Once coatings were developed, materials were evaluated for rate capability, capacity, and temperature performance. Overall, no clear trend was observed for battery capacity or rate capability between the three different materials suppliers. The temperature range tested was between -40 °C to 60 °C, where no clear trends were observed. Figure 19 shows the performance comparison for three different materials suppliers at a variety of different discharge rates and fluorination levels. All batteries were assembled and tested using the same protocols and electrolyte to minimize variations due to laboratory practices.

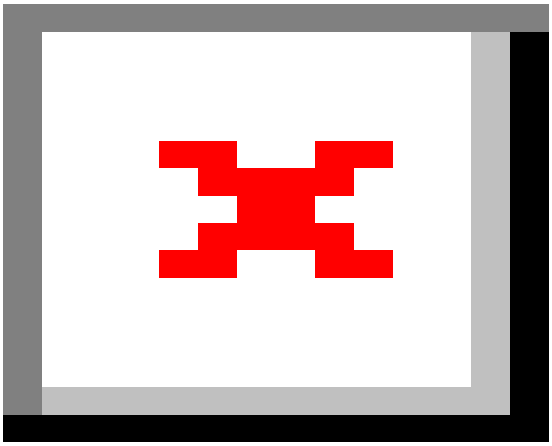

Figure 19. Evaluation of commercially available materials for the CF_x primary battery system. Materials were evaluated at several different rates and at several different fluorine levels. Overall, very little variation in specific energy density for the different materials (inset).

The identification of materials available for this study was unable to identify a clearly superior material for evaluation. Therefore, materials were selected and used based upon availability in the laboratory and not on performance.

3.1.1. Novel methods for evaluation of material functionality

In an attempt to identify new methods for materials evaluation, particularly with respect to the dissolution and reduction of available lithium within the CF_x system, several different states of charge and lithiation levels using several different CF_x electrodes were fabricated and evaluated as prepared or discharged to zero state of charge. These materials were then harvested by disassembly of the coin cells and subsequent rinsing with dimethyl carbonate (DMC) to clean the surface of the electrode and offer a salt-less sample. These samples were then evaluated for magnetometry response. Ideally, a clear difference will be observed for the lithiated CF_x samples as opposed to non-lithiated samples. If so, this can potentially become a screening metric for binding agent efficiency, as less-effective binding agents will show a lower differentiation for lithium under magnetic moment measurements. Due to time, only initial data will be shown for magnetometry measurements.

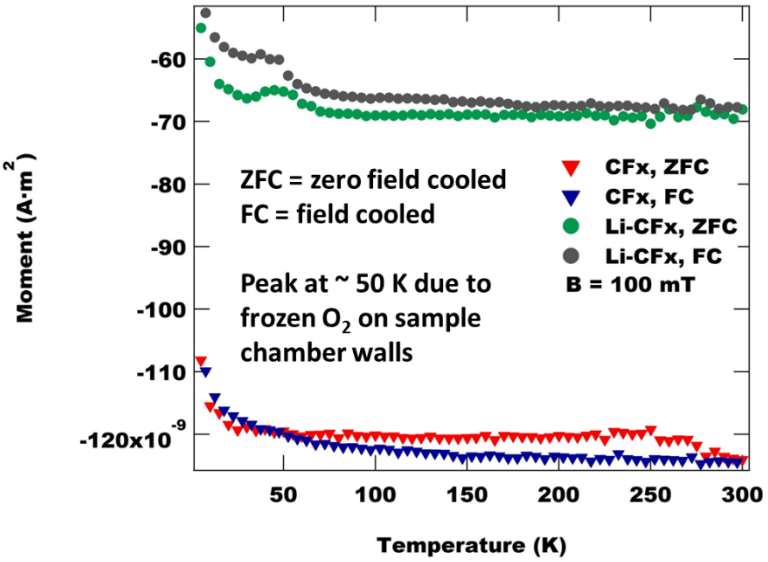

Figure 20. Magnetometry data for carbon monofluoride samples that were as prepared (non-lithiated) or fully discharged (lithiated).

Samples were tested in situations with both active field cooling (denoted FC) and without active field cooling (denoted ZFC). Additionally, in this sample preparation, there is some background noise present, which shows up as a weak magnetic signal. The overall signal from these samples is diamagnetic, which is likely due to a significant contribution from the sample holder. These samples utilized a plastic screw cap sample holder in an effort to create a hermetically sealed environment for materials evaluation. From the results shown in Figure 20, it is clear that there is an increase in the paramagnetic moment in these samples (decreased diamagnetism) from the introduction of lithium into the system. This evaluation technique for lithium primary and second electrodes is currently a much underutilized technique for understanding battery mechanisms and lithiation. By utilizing magnetometry techniques to evaluate the lithiation of electrodes utilizing different anion binding agents, it could be possible to quantify the efficiency of lithium fluoride dissolution (or other salt species). Unfortunately, due to data acquisition considerations, this is not necessarily an in-situ technique but it can definitely be used to understand the efficiency and mechanism for discharge in many of the complication solvent/cathode interactions that we are researching for this program.

3.2. Identification and evaluation of potential co-solvents

This work focuses on evaluating dimethyl methylphosphonate (DMMP) solvents in conjunction with tris(pentafluorophenyl) borane (TPFB) bound to LiF, which is supplementary to previous efforts to understand ABA performance in nonflammable solvents [13-15]. DMMP has been studied extensively by others as fire retardant in Li-ion cells [19, 31-33]. Pairing DMMP with TPFB-LiF synergistically endows the cell chemistry with both enhanced thermal stability and improved electrochemical performance. The majority of these studies were preformed using the materials previously identified in an effort to use nothing but commercially available materials with optimal performance.

The propensity of the ABA to dissolve LiF has been taken advantage of for improving Li-ion cell performance before. For example McBreen proposed the use of ABAs, also known as anion receptors, to dissolve the accumulated LiF, due to the decomposition of the LiPF6 salt, on cathode surface in Li-ion batteries [20]. He demonstrated that the cathode can be rejuvenated by dissolving the LiF layer. West [21] et.al. have demonstrated reversible intercalation of F^- in graphite from an organic solution containing an ABA and LiF. However, our work focuses on dissolving the generated LiF in the Li-CF_x discharge to improve the ohmic and interfacial resistances as the cell discharge. We are accomplishing these by varying the composition of the ABA-LiF complex salt in the electrolyte. In this paper we will discuss the thermal and the electrical properties of the DMMP/ABA-LiF electrolyte and the electrical performance of CF_x materials obtained from different vendors in the above electrolyte.

3.2.1. Experimental

Several CF_x powders were obtained both through purchase and free from several vendors. For te purposes of discussion, these materials are designated as A, B, C and D. The solvent DMMP (99.5% purity) was purchased from PFALTZ-Bauer and used as received (see Figure 21), the TPFB ABA (Figure 21) was synthesized by Richman Chemicals under a Sandia contract, and the LiF was purchased from Fischer Scientific (>99.95 purity). The ABA, LiF, and CF_x were all used as received but were baked out under vacuum overnight at 110 °C before coating into electrodes. Three different electrolytes containing DMMP solvent with 1M TPFB and 1M LiF, 0.5M LiF or 0.1M LiF were prepared in an argon filled glove box. CF_x electrodes were made as described elsewhere [34]. The electrode composition is 94:3:3wt% (active material:PVDF:Denka Carbon). All electrolytes were made fresh as and when required. 2032 coin cells were fabricated in a dry room with a dew point below -40 °C. Electrodes of 0.625" diameter were punched and assembled in a 2032 half-cells and crimped in a Hohsen automatic machine after adding the electrolyte. Cells were evaluated using a series 4000 Maccor tester and impedance was collected using a 1287 Electrochemical Interface/1260 Solatron Impedance Phase Analyzer stack. The electrolyte flammability was evaluated in a home-built apparatus at our thermal abuse facility. Differential scanning calorimetry (DSC) was performed using a TA Instruments Q2000 calorimeter to evaluate the thermal response for the ABA materials and electrolytes. Approximately 10 mg of material was sealed in a high-pressure stainless steel DSC pan under inert atmosphere.

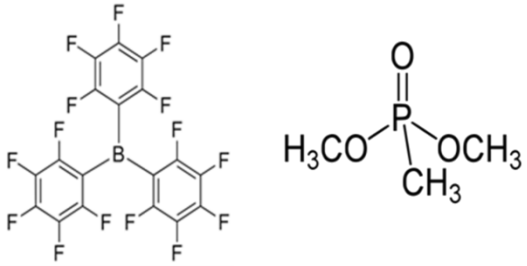

Figure 21. Structure of the TPFB ABA salt and DMMP solvent.

3.2.2. Results and Discussion

3.2.2.1. Conductivity of electrolytes

Electrolytes consisting of DMMP, 1M TPFB, and xM LiF where x=1, 0.5 and 0.1 were prepared for evaluation and kept under argon until coin cells were fabricated. Figure 22 shows the relationship between temperature and conductivity for electrolytes containing 1M (red), 0.5M (green), and 0.1M (purple) LiF. As expected, the conductivity increases with increasing concentration of LiF. Generally, the difference between conductivity values increases with increasing temperature and decreases with decreasing temperature. The conductivity for the 1M LiF is comparable to that of the conventional battery electrolytes [35]. Figure 23 shows electrochemical voltage window for two electrolytes recorded at a 2 mV s^{-1} scan rate. The voltage traces show similar electrochemical characteristics for both DMMP 1M TPFB:1M LiF and DMMP 1M TPFB:0.5M LiF. Both electrolytes show little electrochemical activity throughout the scanned voltage range, indicating stability up to 3.5 V vs. Li/Li^+. The voltage was not scanned beyond 3.5 V since this is higher than the cell voltage for this electrochemical couple. However, it has been shown that this type of electrolyte is stable at voltages > 4.2V [31].

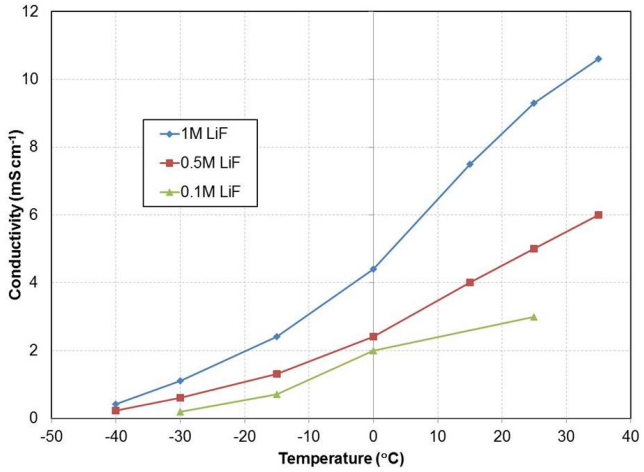

Figure 22. Conductivity comparison for electrolytes containing 1M TPFB ABA with 1M LiF (blue), 0.5M LiF (red), and 0.1M LiF (green).

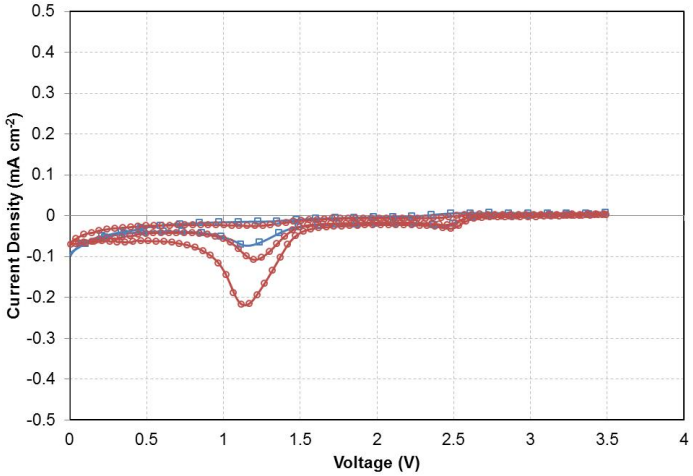

Figure 23. Electrochemical voltage stability window comparison for DMMP-1M TPFB:1M LiF (blue), DMMP 1M TPFB:0.5M LiF (red).

The reductive peaks, one at ~1.25 V and the other at ~2.5 V, decrease quickly with cycling and were not investigated further. However, likely reasons for these peaks may be associated with the impurities of the pentafluorobenzene boronic acid (98% pure) or the presence of gaseous species in the electrolytes. Voltage trace for the DMMP 1M TPFB: 0.1M LiF (not shown) are consistent with those reported in Figure 23.

3.2.2.2. DSC measurement

DSC measurement was performed on the ABA salt to evaluate the thermal stability of the material at elevated temperatures. DSC trace in Figure 24 clearly demonstrates that TPFB ABA is stable up to ~340 °C. The endotherm at 109 °C corresponds to the melting of the compound and the exotherm at high temperature corresponds to the decomposition of the material (similar behavior was observed for other ABAs by us and others) [36]. The high temperature stability of the ABA material enhances the overall thermal stability of the DMMP electrolyte, which has consequences for high rate thermal runaway for cells constructed with these materials.

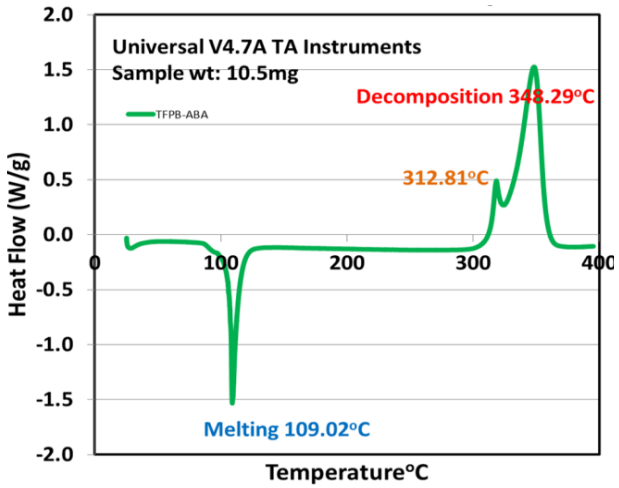

Figure 24. Differential scanning calorimetry (DSC) response for the TPFB ABA material.

3.2.2.3. Thermal ramp

At our thermal abuse facility we have a home-built fixture for performing thermal ramp test. This setup consists of a copper block with a pre-drilled hole to accommodate an 18650 cell and two smaller holes for heater cartridges. The line drawing on the right shows the positions of thermocouples in the copper block and the spark source above it. An 18650 cell filled with ~ 5 mL of electrolyte is sealed, crimped, and inserted into the center hole in the copper block. The copper block is heated at a predetermined rate and a spark source positioned above the copper block is turned on to ignite solvent vapor. Flammability test are conducted in this manner for very specific reasons. The positioning of all components in this test (including the electrolyte volume) mimics the worst-case scenario for a battery field failure. Several standard flammability tests have been reported and are commonly conducted for battery electrolytes, but they do not necessarily accurately recreate the failure mode of a field failure in which heated cells vent into a potential spark or flame source.

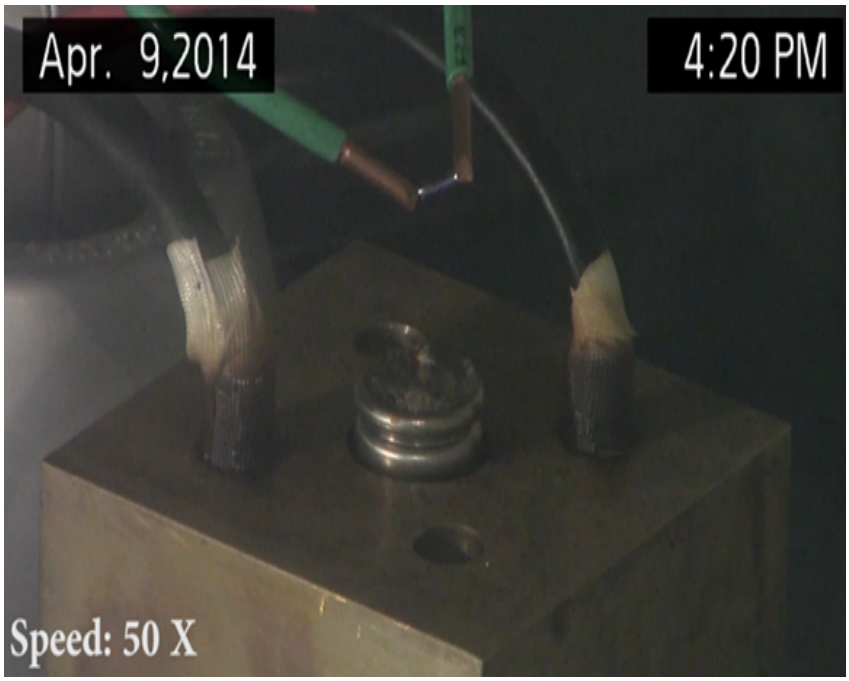

Figure 25. Response from thermal ramp testing of the DMMP-1M TPFB:1M LiF electrolyte.

Thermal ramp measurements were conducted on DMMP 1M TPFB:1M LiF electrolytes and a screen capture during the test is shown in Figure 25. While a puddle of electrolyte bubbling on the neck of the cell can't be seen clearly, the figure clearly shows the spark from the spark source above the cell. Any electrolyte vapors that are released from the cell hardware will be directed into the spark source. This test resulted in no ignition or combustion of any material from the cell. The measurement was repeated to ensure reproducible nonflammable behavior. After characterizing the electrolytes for both thermal and electrical properties, discharge and impedance characteristics were evaluated.

3.2.2.4. Discharge behavior of CF_x based cells

Figure 26 shows voltage vs. specific capacity traces for 4 different materials evaluated in this study. The performances for B and C are comparable and they showed flat voltage profiles for the majority of the discharge. Performance of A is very similar to B and C but exhibits a higher average voltage. Material D starts off at a higher voltage compared to the rest but shows decreasing voltage slope as the discharge progresses. All materials have similar particle size distributions, centered at 10 μm average particle size. Figure 27 shows cell voltage vs. capacity for material C in DMMP – 1M TPFB electrolyte with varying concentrations of LiF. The initial voltage drop is the highest for the electrolyte containing 0.1M LiF, followed by 0.5M LiF, and the smallest for the 1M LiF, which is the converse of the trend that we see in electrolyte conductivity. The other materials tested exhibited similar trend in voltage.

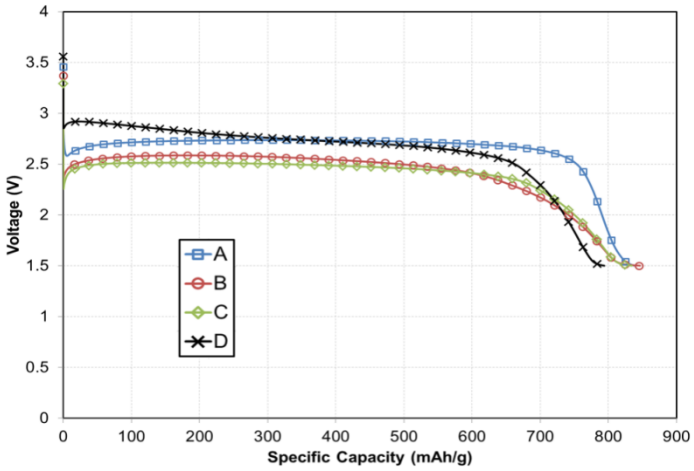

Figure 26. Characteristic discharge behavior for CFx materials from several different suppliers. Cells utilized DMMP – 1M TPFB:1M LiF electrolyte and were discharge at a C/100 rate.

Although the voltage drop is most severe for the 0.1 M LiF, as discharge progresses the voltage rises faster than the other LiF concentrations and eventually surpasses the 1 M LiF at around 300 mAh g^{-1}. The behavior for the 0.5 M LiF is similar except that it caught up with the 1M at around 444 mAh g^{-1}. The discharge specific capacities for the 1 M; 0.5 M and 0.1 M LiF concentrations are: 727, 751, and 779 mAh g^{-1} respectively. We believe that the improved performance of the 0.5 and 0.1M LiF can be contributed to the simultaneous decrease in the ohmic and interfacial resistances due to the dissolution of the LiF generated in the discharge reaction by the excess ABA in the solution. In general, of the two factors, the impact of the interfacial resistance on cell performance may be more important than the decrease in the ohmic resistance since the interfacial resistance generally dominates the cell impedance and consequently it determines the slope of the discharge curve [37, 38]. For larger interfacial resistances the slope of the curve will also be larger. The computed the slope ($\Delta V/\Delta T$) from the V vs. time plots (not shown here) for the three discharge curves was computed. The magnitude of the slope is the largest (0.272 V h^{-1}) for the 1M LiF followed by 0.244 V h^{-1} for the 0.5M LiF and 0.227 V h^{-1} for the 0.1 M. To verify if the ohmic and interfacial resistances decrease with discharge for the 0.5 M and 0.1 M LiF we performed impedance measurements at different depth of discharge (DOD) conditions.

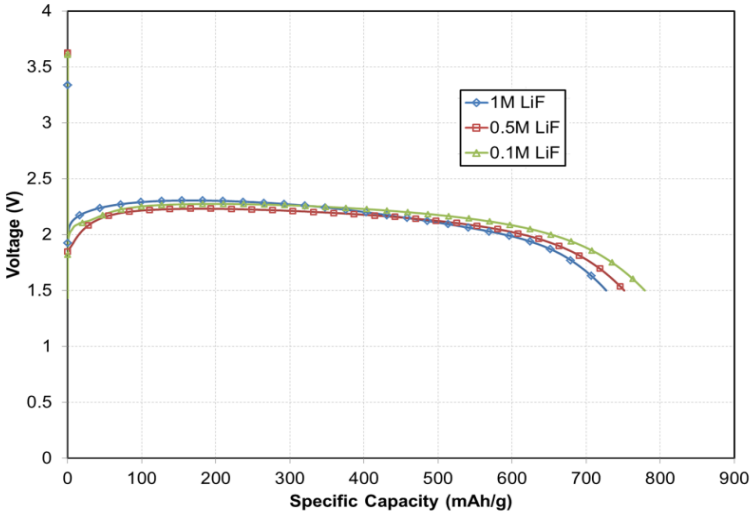

Figure 27. Specific discharge capacity for DMMP – 1M TPFB with varying concentrations of LiF salt at a C/5 discharge rate.

3.2.2.5 Impedance Studies

Electrochemical impedance spectroscopy (EIS) of cells was collected at different depth of discharge (DOD). Figure 28 shows Nyquist plot of cell impedances for material C1 at different DODs for the DMMP 1M TPFB:1M LiF and DMMP 1M TPFB:0.5M LiF electrolytes. For the 1M LiF, the interfacial impedance increases with DOD and for the 0.5M LiF it decreases with DOD. This observation agrees with our prediction based on the discharge profile of the cell (shown in Figure 27) and this trend is also seen in the DMMP 1M TPFB:0.1M LiF sample (not shown). Figure 29 shows the high frequency impedance data as a function of DOD for the 1M LiF and 0.1M LiF. The ohmic resistance decreases with discharge for 0.1M LiF and remains constant for the 1M LiF. This indicates that the 1M LiF electrolyte does not exhibit ohmic resistance changes during discharge while the 0.1M LiF electrolyte decreases as the cell discharges.

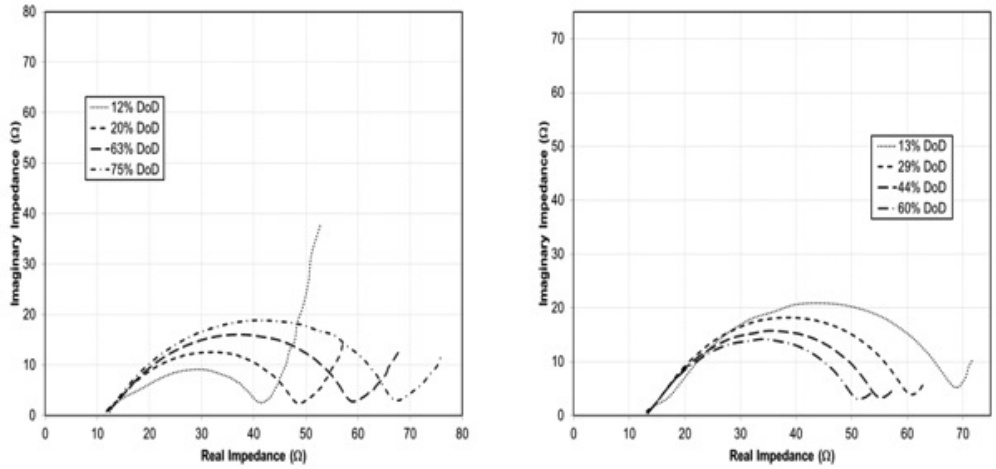

Figure 28. Nyquist plot showing the impedance response for cells at increasing depth of discharge for DMMP – 1M TPFB:1M LiF (left) and 1M TPFB:0.5M LiF (right).

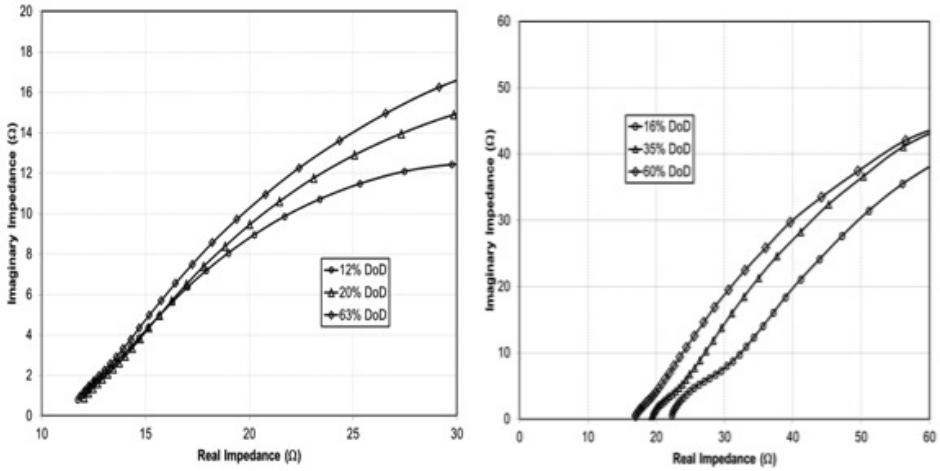

Figure 29. Ohmic resistance variation with varying depth of discharge for DMMP 1M TPFB:1M LiF (left) and DMMP 1M TPFB:0.1M LiF (right).

3.2.3. Identification and evaluation of potential co-solvents conclusion

Cells containing sub-stoichiometric amounts of LiF in the electrolyte were demonstrated to perform slightly better than cells containing a 1:1 molar ratio of ABA: LiF by delivering slightly higher capacity. The benefits were shown to correlate to the reduction of both interfacial and ohmic impedance within the cell. Observation of higher capacity and lower interfacial resistance agrees with our prediction that de-fouling the cathode pores of LiF should lead to better performance. Demonstration confirms that the ABA in solution is capable of directly defouling micro porous electrodes, which has implications for not just lithium primary cell chemistry. The ABA was found to be stable up to 340 °C and was shown to be nonflammable during thermal flammability testing. These results can be implemented in real world applications by optimizing ABA:LiF ratios to maximize the gains in cell performance.

3.3. ABA linked siloxane and liquid ABA based systems

During the study of the various synthesis methods for both anion binding agents and their subsequent linkage to siloxane based electrolyte backbones, two materials were identified as new and un-discovered electrolytes. These two materials can be seen in Figure 14 compound #32 for the siloxane linked ABA materials and in Figure 15 compound #36 for the liquid phase fluorous ABA. Due to limited literature reports regarding novel ABA compounds, the material seen in Figure 15 compound #36 was of particular interest as there is no other mention of room temperature liquid phase ABA materials. Additionally, the scale up and synthesis of the siloxane linked material seen in Figure 14 compound #36 (see Figure 30) has potential to be a new electrolyte material that has not been reported in current literature.

Figure 30. Scaled up synthesis of siloxane linked ABA materials, as seen in Figure 15 compound #36.

Synthesis of these materials was conducted as described previously. The siloxane linked ABA materials do appear to have difficulty with the purification steps at the end of their synthesis (see Figure 14, synthetic transitions from compound 30 through 32). Because of the low yield during these steps, the compound preceding the ABA linkage (Figure 14 compound 30) was also investigated as a stand-alone electrolyte for lithium based battery systems (see Section 3.4).

Electrochemical stability was evaluated for several of the synthesized materials. A representative cyclic voltammogram for these can be seen in Figure 31. This shows the electrochemical stability of the siloxane linked ABA materials in the absence of lithium-based salts. As expected, the response for these materials is mostly resistive with a small capacitive contribution from the double layers present in the measurement. The electrochemical stability window for these materials also extends up to at least 4.5V, which is much larger than the range needed for the CF_x lithium primary battery system. This at least indicates that this electrolyte may be suitable for not only current lithium ion systems (those with an approximate 4.2V working window) but also future high voltage systems like the spinel systems with working voltages up near 4.6 V.

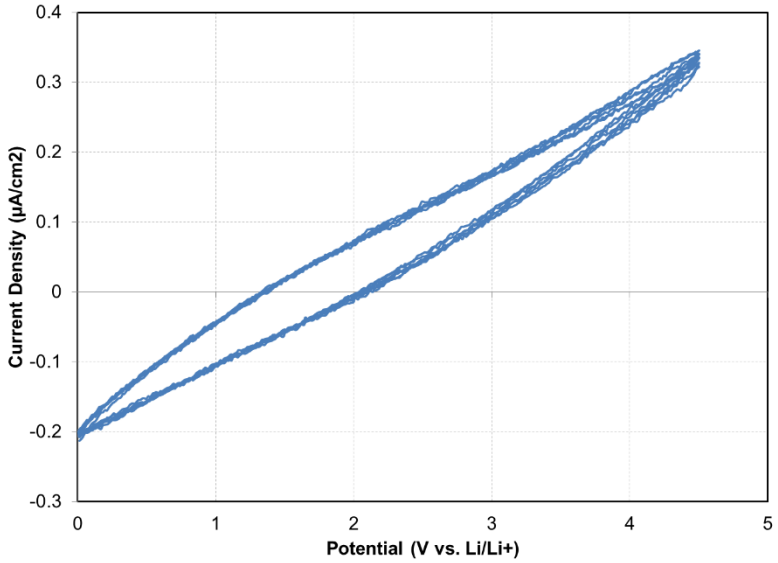

Figure 31. Cyclic voltammetry of the siloxane linked ABA materials using a BASi glassy carbon electrode for both the working and counter electrode. Lithium was used as a reference electrode for these measurements.

In order to evaluate the thermal stability of the synthesized materials, differential scanning calorimetry (DSC) was performed as described in Section 3.2.2, where approximately 10 mg of material was sealed into a high temperature DSC pan (to prevent pan rupture during evaluation) and the temperature was ramped from ambient to 400 °C. DSC traces for both the siloxane linked ABA and the liquid phase ABA can be seen in Figure 32.

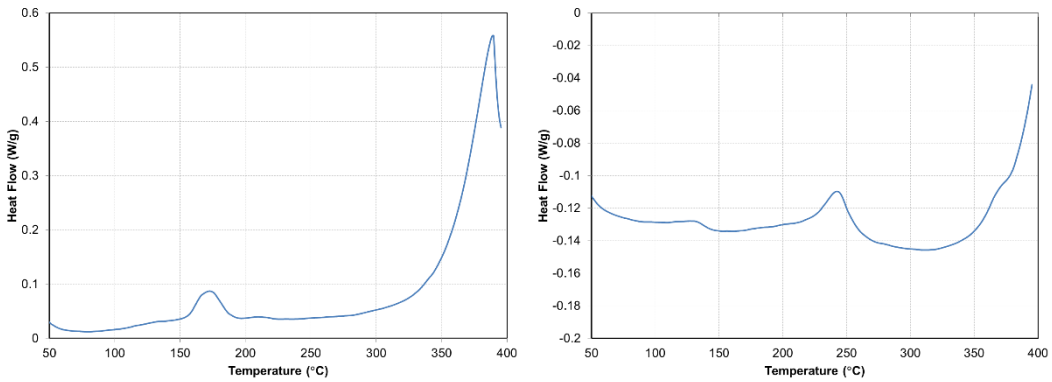

Figure 32. DSC evaluation of both the siloxane linked ABA materials (left) and the liquid phase standalone ABA (right). Evaluation was completed on a TA Instruments Q2000 at 10 °C/min from ambient to 400 °C.

It is apparently that both the siloxane linked ABA and the liquid phase ABA materials that were synthesized are very thermally stable. Both indicate exotherms at temperatures above 350 °C. Both materials exhibit a very small exotherm peak at ~175 °C and ~240 °C, but complete breakdown of the material does not happen until elevated temperature as compared to currently used electrolytes (Figure 33).

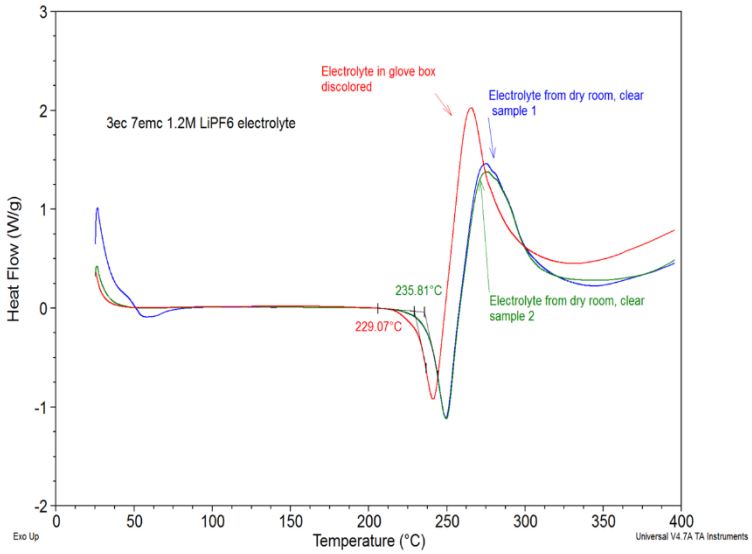

Figure 33. DSC trace for standard EC:EMC (3:7 wt%) with 1.2M LiPF6. Several traces are shown, all of the same material from different batches. All show onset of degradation at approximately 230 C and have a much larger overall heat flow during exothermic reactions than the ABA based materials.

Electrochemical cells were fabricated using these materials to evaluate their ability to support discharge current in full cells containing carbon monofluoride cathodes and lithium anodes. Electrodes were coated with a ratio of 94:3:3 CF_x active material:Kureha PVDF:Denka conductive carbon on a reel to reel reverse comma coater. Electrodes were punched using a 0.625" Di-acro punch and assembled into 2032 coin cells versus ~8 mil lithium anodes. Cells were discharged at approximately C/50 discharge rates to evaluate the difference in polarization of current state of the art electrolytes versus the synthesized siloxane linked ABA materials, as seen in Figure 34.

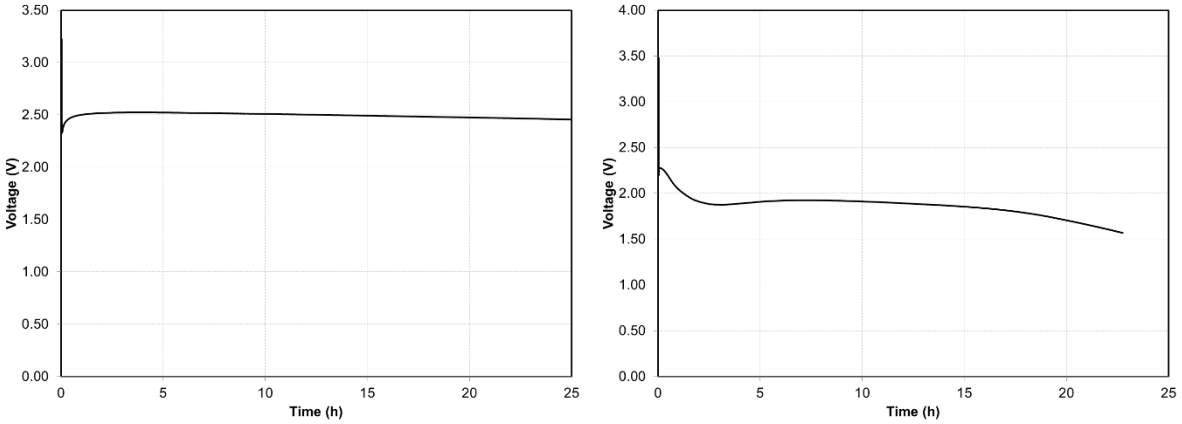

Figure 34. Discharge comparison for CF_x 2032 coin cells using standard 3:7 (w%) EC:EMC based electrolyte with 1.2M $LiPF_6$ (left) versus synthesized siloxane linked ABA materials using 1.2M $LiPF_6$ (right).

While the discharge using the siloxane linked ABA materials shows a high polarization upon application of discharge current, there has been no previous demonstration of electrolyte that is also capable of lithium fluoride dissolution in solution. The capacity of this material (while low) was evaluated to be on the order of tens of millimolar in solution with the solvent alone. While this is lower than was aimed for, it does demonstrate a change in operation for battery electrolytes that moves toward active electrolyte that can support both discharge transport rates and actively work toward increasing battery longevity and electrolyte conductivity.

The primary voltage loss seen in Figure 34 is attributed to the limited dielectric strength of the electrolyte material. The dielectric constant for this material was measured to be 3.01, which is sufficiently low to exclude complete dissolution. Not only does this lead to decreased LiF dissolution initially, but also contributes to an overall increased battery resistance as compared to the carbonate-based systems. As shown later (Figure 37), this effect is not directly a result of lower conductivity but has to have contributions due to dielectric constant. Additionally, the electrolytes used that utilize larger siloxane based materials tend to exhibit higher viscosities, which also contribute to higher cell polarizations. In order to combat these difficulties, many electrolyte blends were investigated to optimize cell performance (as is the common solution for battery electrolytes).

3.4. Acetonide-siloxane based systems

The solvent synthesis and structure is shown in Figure 14, structure 30. The resulting solvent is a clear liquid at room temperature with low viscosity. This solvent proved to exhibit low solubility for Li-salts such as $LiPF_6$ and ABA-LiF. This is primarily due to low dielectric constant. This is consistent with many battery solvents, which is why the typical battery electrolyte contains several solvent species. Each of these solvents is typically responsible for increasing certain performance metrics for the electrolyte. Whether increasing the dielectric constant or lowering the viscosity there are very limited examples of a single electrolyte system that achieve performance anywhere close to multi solvent electrolytes.

The next step was to mix other aprotic solvents including DMMP, F-EC, EMC, DEC *etc.* with this to see if the solvent blends dissolve the salts. These solvent blends dissolved $LiPF_6$ and the

ABA-LiF salts but unfortunately, these did not only phase separate but began to discolor with time. The formulations tested can be seen in Table 1.

Table 1 – Electrolytes Formulations Based on Acetonide-Siloxane Solvent.

Solvent(s)	Salt	Composition	Comment
EC:EMC	LiPF6	(3:7)w% - 1.2M	No discoloration and phase separation
EMC:acetonide-silane	LiPF6	(1:2)v% - 1.2M	Discoloration/phase separation
DEC:acetonide-silane	LiPF6	(1:2)v% - 1.2M	Discoloration/phase separation
DMMP:acetonide-Silane	LiPF6	(1:2)v% - 1.2M	No discoloration/phase separation/gelling out
DMMP:acetonide-Silane	Ox-ABA-LiF	(1:2)v% - 1M	Discoloration/phase separation
F-EC:acetonide-silane	Ox-ABA-LiF	(1:2)v% - 1M	Discoloration/phase separation

For each of the mixtures prepared, the predominant behavior was a phase separation of the two different solvent species. Each of the primary mixtures and their color/phase separation can be seen in Figure 35.

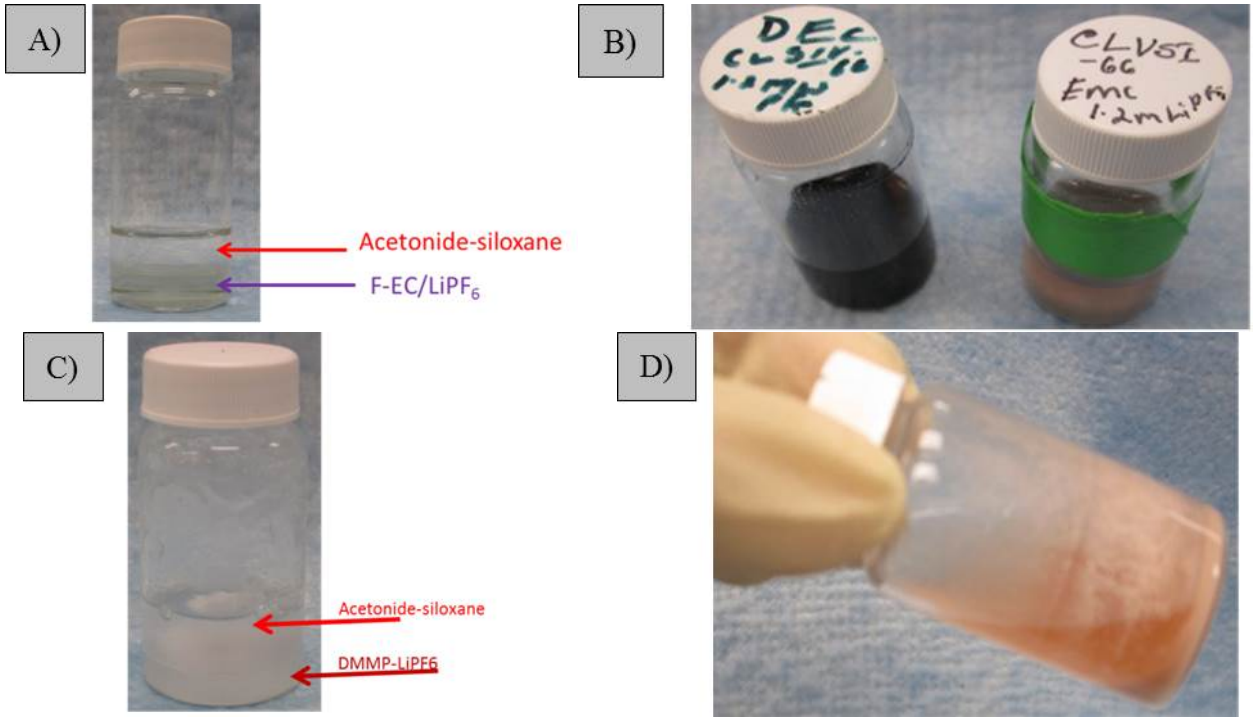

Figure 35. Photographs of several of the acetonide-siloxane based electrolytes. For each of the prepared solutions, it can be seen that discoloration and phase separation are the primary behaviors. This can seen in mixtures of A) acetonide-siloxane:F-EC (2:1 v%) with 1.2M $LiPF_6$, B) acetonide-siloxane:DEC (2:1 v%) with 1.2M $LiPF_6$ (left) and acetonide-siloxane EMC (2:1 v%) with 1.2M $LiPF_6$ (right), C) acetonide-siloxane:DMMP (2:1 v%) with 1.2M $LiPF_6$, and D) acetonide-siloxane:EMC (2:1 v%) with 1M ABA and 1M LiF.

Each of these electrolytes was assembled into 2032 coin cells using ARC CF_x, where x=1.0, to evaluate their ability to support discharge. Due to obvious reaction in solution, it was anticipated that these materials would be highly performing in a full cell. Figure 36 shows discharge capacity comparison at a C/50 rate. The discharge capacity normalized per gram of active

material is plotted in the x-axis. The performance of the control far exceeds that of the acetonide-siloxane containing blends.

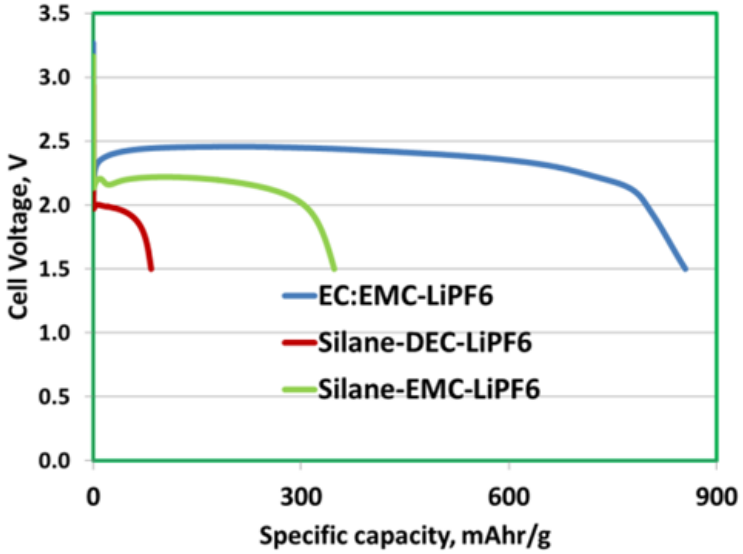

Figure 36. Discharge performance for electrolytes composed of acetonide-siloxane with several other co-solvents using 1.2M $LiPF_6$. The control electrolyte (blue) is EC:EMC (3:7 wt%) with 1.2M $LiPF_6$. Discharge rates were kept at C/50 and calculated from the weight of the cathode active material.

The primary reason for the low specific capacity seen in Figure 36 can be attributed to low conductivity and dielectric constant for these materials. To demonstrate this effect, the material seen in Figure 35D was used to perform electrochemical impedance spectroscopy. This was done using an electrochemical cell containing glassy carbon electrodes with a surface area of 0.07 cm^2 and a gap of 0.2 cm between the electrodes. The frequency was swept from 1 Mhz to 1 hz using a solartron 1287/1260 potentiostat and frequency response analyzer. The resulting impedance for the electrolyte was calculated to be 2 mS/cm at 25 °C as seen in Figure 37. This is not as high as the control electrolytes, indicating that the lower dielectric constant for these materials also directly influences the decreased cell performance. This is also evidenced in the impedance values for the full cells that were prototyped using the same electrolyte. The Nyquist plot of impedance clearly shows that the cell impedance is very high on the order of megaohms (Figure 38). We believe the high impedance is a direct result of the inability of the acetonide-siloxane solvent to dissolve the Li-salt, which is responsible for ionic conduction. This specific high purity siloxane solvent still requires optimized properties for use in batteries, despite promising conductivity and safety performance.

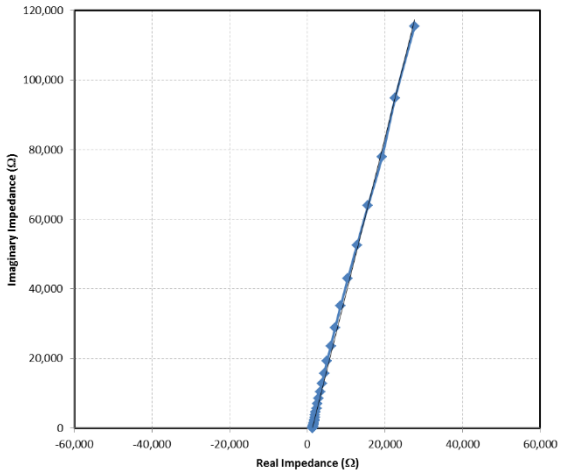

Figure 37. Electrochemical impedance spectroscopy data for acetonide-siloxane:DMMP (2:1 v%) with 1M oxalic ABA and 1M LiF at 25 °C. The resulting electrolyte conductivity for this material is 2 mS cm^{-1}.

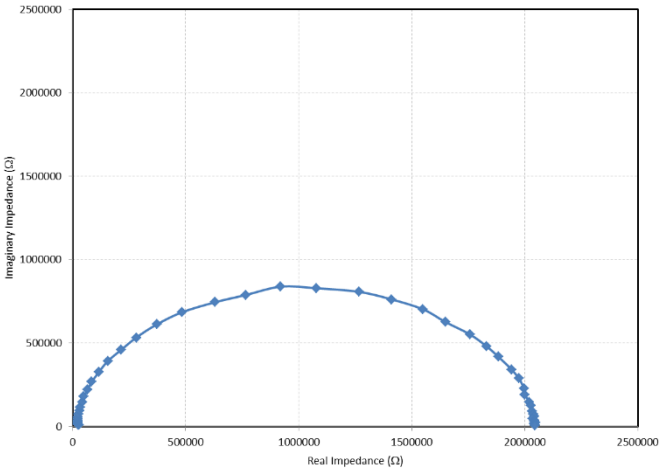

Figure 38. Electrochemical impedance spectroscopy of a 2032 coin cell with a CF_x cathode and lithium metal anode at 3.6 V. The phase separated acetonide-siloxane with 1M oxalic ABA and 1M LiF electrolyte was used.

4. MOLECULAR INTERACTIONS AND SYSTEM MODELING

Theoretical studies focused on high fidelity molecular models of battery components. In one study, *ab initio* methods based on density functional theory (DFT) were used, in conjunction with conductivity measurements, to determine the binding affinities of various anion receptors to fluoride anions. Anion receptors that bind strongly to fluoride anions in organic solvents can help dissolve the lithium fluoride discharge products of primary carbon monouoride (CF_x) batteries, thereby preventing the clogging of cathode surfaces and improving ion conductivity. The receptors are also potentially beneficial to tradition lithium and lithium air batteries.

In another theoretical study, an empirical force field was assessed for its ability to represent the dielectric properties of two cyclic carbonates widely used in battery applications. Solvent dielectric properties are important because ion dissolution and diffusion are correlated with solvent dielectric response. Due to the long timescales involved, empirical force fields are needed in place of ab initio models. Once validated, the empirical models can be used to understand the mechanisms of ion dissolution and transport in battery electrolytes. These models can also be helpful in understanding solid electrolyte interphase (SEI) layers that form in lithium ion batteries.

In the study of anion receptors, a simple oxalate-based pentafluorophenylboron compound was found to bind as strongly, or more strongly, to fluoride anions than many phenyl-boron anion receptors proposed in the literature. Since that receptor is sufficiently electrophilic that organic solvent molecules compete with F for the boron-site, the models required treatment of specific solvent effects to predict F binding affinity accurately. Those effects are generally neglected in the literature, leading to incorrect predictions.

In the assessment of the empirical force field, two dielectric properties were calculated: dielectric constant and dielectric relaxation time. The former measures polarization of a material by a static applied field while the latter assesses the lag of the polarization in responding to a changing applied field. Ethylene carbonate (EC) and propylene carbonate (PC) have high dielectric constants needed for dissociation of lithium salts, but they also have high viscosity that limits the transport of lithium ions. Thus, EC and PC electrolytes are often used with other low viscosity materials to achieve fast ion transport. Since batteries operate at a range of temperatures, the variation in electrolyte properties with temperature is an important consideration in electrolyte development. Our studies found that the predicted dielectric values based on the empirical force field parameters (OPLS-AA) agree well with the few experimental results that have been published.

In future work, we propose to apply our high fidelity molecular models to answer new questions raised during this project. First, the empirical force field models need more rigorous assessment by new measurements of electrolyte dielectric properties at a wider range of temperatures and for mixtures of electrolytes. Then our validated models can be applied to analyze the mechanism of LiF dissolution in bulk solvent and at the interface between electrolyte and electrode where SEI layers form. We hypothesize that, in the absence of anion receptors, LiF dissolution in cyclic carbonate organic solvents is due mostly to the formation of ionic aggregates, not isolated F^- ions. Also, our models can be applied to understand the unanticipated liquid state and ion

scavenging properties of a new anionic binding agent discovered during this project. Finally, the validated empirical models will be used to analyze Li+ transport mechanisms to advance the design of new electrolyte materials for batteries.

4.1. DFT and Conductivity Studies of Boron-Based Anion Receptors [39]

The application of boron-based anion receptors (denoted "ABA" herein) in lithium ion and metal-air batteries has been an area of active research [40-50]. Experimental and electronic Density Functional Theory (DFT) studies of ABAs have been conducted to examine fluoride anion binding affinity, electrolyte conductivity, redox stability, and other properties critical to battery operations.

Boron-based anion receptors often contain strongly electron withdrawing pentafluorophenyl (-C_6F_5) groups. An often-cited example is tris(pentafluorophenyl)borane (TPFPB) [41,43]. ABAs with multiple phenyl groups tend to be bulky molecules, and can yield viscous electrolytes that impede ionic motion. Slow ionic transport adversely impacts rate capability and other functionalities in an electrochemical storage system. In this work, we focus on an oxalate-based "ABAO" (Figure 39a and Figure 41a), with the boron atom bound to only one C_6F_5 ring in addition to two oxygen termini of an electron-withdrawing oxalic group [40, 47]. Using electronic structure Density Functional Theory (DFT) techniques, we predict that the ABAO gas phase F^- binding free energy is comparable to many higher molecular weight anion receptors that have been examined with computational methods [46]. The gas phase energetics of a subset of ABAs taken from Reference [46], depicted in Figure 39 and Figure 41, are re-examined in this work for comparison.

In the presence of liquid solvents, ABAO binding affinity with F^- is found to remain enhanced compared to other ABA's. Here we apply DFT methods to examine how different ABA's and solvent molecules (S) affect the LiF dissolution free energy (ΔG_{diss}), according to:

(1)

The dissolution process can be broken up into steps of a thermodynamic cycle (Figure 40)

(2)

(3)

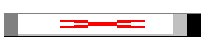

(4)

In the equations above, "(solv)" denotes solvation by the organic electrolyte; its absence means the species is in the gas phase. Standard states (1.0 M concentration) are assumed for Li^+ and F^- ions, even when they are considered heuristically to exist in the gas phase. Gas phase contributions to entropy ultimately cancel in Equations 2–4 to recover Equation 1. The free

energy change in the first step (Equation 2) describes solid LiF splitting into ions in the gas phase (ΔG_{LiF}). The free energy for solvation of Li^+ ion (Equation 3) is quantified by $\Delta G_{solv-Li^+}$. The free energy in the last step (Equation 4) describes binding of solvated ABA to F^- (ΔG_{F^-}). The LiF solubility or dissolution constant (Equation 1) in the presence of different ABAs is defined as:

(5)

(6)

where Boltzmann's constant (k_B) and the absolute temperature (T) define the energy scale, and the dimensionless ion concentrations are normalized by 1.0 M, consistent with the 1.0 M concentration reference systems in our calculations. We also present corroborating experimental data that demonstrate the improvement of electrolyte conductivity when ABAO is present.

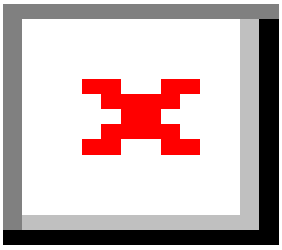

Figure 39. Structures of (a) oxalic (ABAO), (b) malonic (ABAM), and (c) maleic (ABAE) acid-based ABAs; phenyl boron-based (d) ABA12, and (e) ABA21 proposed in Reference 52; and (f) ABAT. Here the number in ABA*X* refers to the ordering used in Reference 52. Boron atoms are sp^2 hybridized and reside in planar geometries except in ABAT, where B protrudes slightly out of the plane formed by three O atoms. ABA15 of Reference 52 is similar to ABA12, but with the CF_3 groups replaced by CH_3.

Another anion receptor we highlight in our theoretical studies is a recently proposed, geometrically constrained boron ester [44]. In traditional ABAs, the B atom exists in a planar, 3-coordinated geometry and exhibits sp^2 hybridization, but becomes sp^3 hybridized when bound to F^- (Figure 41). The structural changes upon formation of the B-F bond lead to "reorganization

energy" penalties (in analogy with electron transfer reactions [51-52]) that reduce F^- binding affinity (ΔG_{F^-}) [59]. Note that the analogy to electron transfer reorganization energy (λ) is only qualitative. λ is obtained from the difference between vertical and adiabatic e– transfer. Nuclear degrees of freedom are frozen and allowed to relax in the two cases, respectively. In contrast, "vertical" F - binding with a frozen ABA configuration cannot be unambiguously defined. By constraining boron in a non-planar geometry even in the absence of F^-, one of the anion receptors of Shanmukaraj et al. (Figure 39f, hence- forth referred to as "ABAT") is found to exhibit a gas phase F^- binding affinity that exceeds those of planar boron molecules by more than 1 eV (~ 23 kcal/mol or 96 kJ/mol). We only consider the ABAT monomer, not its dimerized/trimerized complexes.

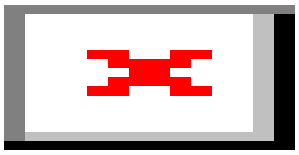

Figure 40. Thermodynamic cycle schematic. The lower and upper halves pertain to ABA anion receptors that bind or do not bind covalently to a solvent molecule ("S"), respectively. Brackets indicate the phase (solid or solvated); their absence denotes gas phase. Relevant equations in each step are labeled.

For strong F^- anion receptors like ABAT, we show that it is crucial to include explicit solvent molecules to predict F^- binding affinity. Consider the following possible intermediate steps toward LiF dissolution implicit in Equation 1:

(7)

(8)

(9)

"S" is a solvent molecule at its liquid density [53]. Equation 8 (same as Equation 4) is pertinent to weak anion receptors that do not coordinate to "S." However, the affinities of ABA toward F^- and solvent molecules tend to be correlated: electrophilic anion receptors that bind strongly to F^- also naturally coordinate to organic solvent molecules with nucleophilic oxygen- and nitrogen-containing terminating groups [54]. Our work will show that Equation 7 is thermodynamically favored by a substantial amount for ABAO and ABAT. Therefore the exchange reactions of Equation 9 must be used to predict net F^- binding free energies for these receptors instead of Equation 8. Such specific solvent binding effects can reduce the selectivity of different ABAs, and can even reverse the ordering of their F^- binding affinity.

Therefore, we also apply DFT methods to survey the interactions of ABAs with four different solvent molecules (Figure 42): acetonitrile (CH_3CN), dimethyl sulfoxide (C_2H_6SO, DMSO), dimethyl carbonate (C_3H_6O, DMC), and ethylene carbonate ($C_3H_4O_3$, EC). CH_3CN is a standard solvent used for experimental and computational benchmarking [46, 55, 56]. DMSO is used in our synthesis of ABAs (see below). EC and DMC are co-solvents in standard lithium ion battery electrolyte. Even after subtracting large offsetting ABA-S binding free energies, ABAO and ABAT are still predicted to be the most thermodynamically favorable F^--binding receptors. In terms of kinetics, strong ABA-S interactions may hinder F^- uptake. This is not the focus of our studies. However, we will report experimental evidence of residual ABA-DMSO complexes.

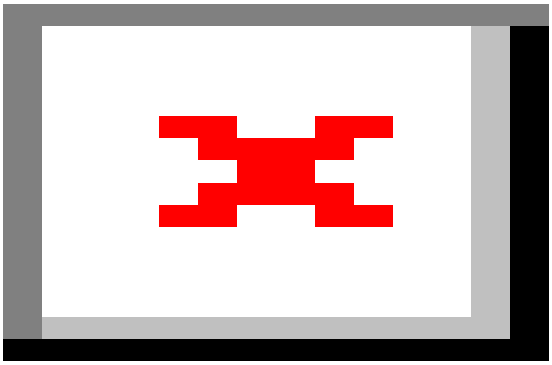

Figure 41. Optimized structures for (a) ABAO, (b) ABAM, (c) ABAE, (d) ABA12, (e) ABA21, and (f) ABAT, all bonded to an F^-. Boron atoms are sp^3 hybridized in tetrahedral-like geometries. Grey, red, white, lime green, and purple spheres represent C, O, H, B, and F atoms, respectively.

In the theoretical literature, the word "solvent" has been used to describe very different types of solvation models. In the Method section, we distinguish between three treatments of solvation, and emphasize the difference between our solvation model and the one applied in the literature [46].

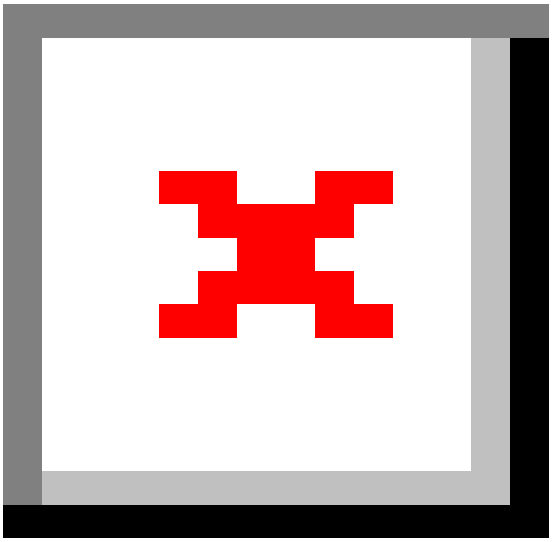

Figure 42. Optimized structures for (a) ABAO-CH_3CN, (b) ABAM-CH_3CN, (c) ABAT-CH_3CN, (d) ABAO-DMC, (e) ABAO-DMSO, (f) ABAO-EC, (g) ABAO- $CH_3CN(CH_3CN)_5$, (h) $LiF(EC)_3$, and (i) $Li_2F_2(EC)_4$. Grey, red, white, lime green, purple, yellow, blue, and dark blue spheres represent C, O, H, B, F, S, N and Li^+ atoms, respectively. Figure 42D depicts DMC in its *cis-trans* conformation, which is most favorable after binding to ABAs, although unbound DMC is most stable as a *cis-cis* conformer.

Finally, the reorganization energy issue mentioned above is one reason that computational design and/or screening of F^- anion receptor may be challenging unless F^- ions, and in appropriate cases, solvent molecules, are explicitly included in the calculations. We have compared several attributes of ABAO, ABAM, ABAT, ABA12, and ABAE, including several internal angles, their HOMO-LUMO gaps, and dipole moments, prior to binding to F^- or solvent molecules. No clear trend or linear correspondence between these attributes and the F^- binding affinity is discernable. Thus the best way to computationally screen F^- binding affinity is to include F^- explicitly in the calculations.

4.1.1. Methods for theoretical studies of boron-based anion receptors

Gaussian suite of programs – Most calculations are conducted using DFT with the PBE0

functional [57]. The Gaussian (G09) suite of programs [58] and a 6-31+G(d,p) basis are used for geometry optimization of molecular clusters and for computing zero-point-energy (ZPE)/finite temperature corrections. The final, single point energy of each cluster is evaluated using a 6-311++G(3df,2pd) basis at the optimized geometry.

In Equations 7, 8, 9, "ABA" can be ABAO, ABAM, ABAE, ABA12, ABA15, ABA21, or ABAT, and the solvent "S" is either CH_3CN, DMC, DMSO, or EC. Here the number in ABA *X* refers to the ordering used in Reference [46]. When Equation 8 is used, the ABA boron-site is not bonded to the solvent molecule. In contrast, on the right side of Equation 7 and the left side of Equation 9, a B-S chemical bond appears. In general, only the one solvent molecule that bonds covalently with boron appears in each calculation. In the case of CH_3CN, a larger explicit solvation shell is included as a check.

The polarizable continuum model (PCM) [59] is used to approximate spectator solvent molecules in the outlying bulk electrolyte region surrounding the cluster made up of ABA and solvent molecule(s) in the G09 DFT simulation cell. Various static dielectric constants (ε_o) are used to mimic different experimental conditions. Since battery electrolytes typically consist of mixed solvents plus salt, we apply $\varepsilon_o = 40.0$ to the outlying region of all these solvent molecules to mimic a uniform, high-dielectric liquid environment. We also consider pure CH_3CN, DMSO, DMC, and EC solvents, with ε_o taken to be 46.7, 35.7, 3.1, and 40.0, respectively. EC is a solid and $\varepsilon_o \sim 40$ is adopted to reflect a reasonable value for EC/DMC mixtures. Finally, each CH_3CN, DMSO, EC, DMC molecule, and F^- anion at 1.0 M concentration, is assumed to occupy a volume of 86.7, 118, 111, 139, and 1668 $Å^3$, respectively. These values are deduced from densities/concentrations at room temperature. In the case of EC, the value comes from the solvent density at higher temperature. The volumes lead to small, < 0.16 eV modifications of default translational entropies reported by the G09 software for pressure equal to 1 atm standard state reaction gas phase conditions.

Different organic solvents solvate Li^+ to different extents (Equation 3), and Li^+ solvation free energies are calculated using Li^+S_4 clusters, with "S"=CH_3CN, EC, DMSO, and DMC. Four explicit solvent molecules are included because Li^+ is generally 4-coordinated in polar solvents [55, 60-65]. In all cases, we report results associated with the bare, unsolvated F^-. These unsolvated F^- ions appear only in inter- mediate steps in the calculations, not the final result (Equation 1). The anion is expected to exist either as LiF solid or ABA-F. The one instance where the free energy of solvated F^- is needed is when predicting LiF solid solubility in liquid electrolyte in the absence of ABAs, for comparison purposes. Even in this case, we find that F^- should exist as $(Li^+)_n/(F^-)_n$ aggregates (e.g., Figure 42(h) and Figure 42(i)).

Putting these considerations together, the total LiF dissolution re- action free energies (ΔG_{diss}) in Equation 1 are calculated using either of the following equations:

(10)

(11)

depending on whether the ABA in question forms a thermodynamically stable complex with the solvent "S."

To assess basis set superposition effects (BSSE) when using the 6-311++G(3df,2pd) basis, standard BSSE corrections are calculated for four gas reactions: ABAO+EC→ABAO- EC, ABAM+EC→ABAM-EC, ABAO+F^-→ABAO-F^-, and ABAM+F^-→ABAO-F^-. The values are 0.07, 0.07, 0.15, and 0.15 eV, respectively. Thus BSSE does not appear to change the preference for EC and F^- binding among different ABAs. The maximum impact on net ABAO-F^- binding, via Equation 9, is 0.08 eV, or ~3 k_BT. Since it has been suggested BSSE calculations can be overestimated [66, 67], and such calculations cannot be performed in the presence of a dielectric environment (PCM solvation method, see below, which should contract the F^- electron cloud and reduce BSSE), we have not conducted BSSE calculations for other ABA's and solvent molecules or included BSSE in the Results section.

Different types of solvation models – It is important to distinguish explicit versus implicit solvent treatments in atomistic length- scale simulations. Most electronic structure (e.g., quantum chemistry or DFT) calculations involve localized basis sets, and a small molecular cluster representing the chemical reaction zone. The cluster is relaxed to its most stable atomic configuration as though it is at zero temperature (T= 0 K). The effect of a finite temperature is typically approximated, post-processing, using a harmonic expansion to account for vibrational motion [68] and by adding translational/rotational entropies. The outlying region containing liquid solvent is treated implicitly, using dielectric continuum (solvation reaction field) methods [59]. If the cluster or reaction zone contains no explicit solvent molecule, the solvation treatment is henceforth de- scribed as "type 1." If at least one solvent molecule is included, it is dubbed "type 2."

A more costly approach, which in principle involves fewer approximations, is ab initio molecular dynamics (AIMD, also known as DFT-MD) [69]. All atoms, including solute and solvents, are treated at the same DFT level, and periodic boundary conditions are generally applied. The simulation is conducted at finite temperature via solving Newton's equation of motion. This approach ("type 3") avoids the arbitrary demarcation of explicit and implicit solvent regions, and is in principle exact given sufficiently large simulation cells, long simulation times, and accurate DFT functionals. In contrast, while more solvent molecules usually give improved results with type 2 solvation [70], this is not guaranteed. In the limit of a large number of solvent molecules, the nature of the geometry optimization used with type 2 means that the most stable state of the system should be a crystallized solid of solvent molecules embedding the solute as an impurity. This clearly does not describe a liquid state configuration. Furthermore, type 2 calculations typically treat finite temperature effects via harmonic expansions even when the pertinent solvent motion is diffusive. This approximation can exaggerate the contribution of zero-point energies.

An alternative to DFT-based AIMD is to conduct molecular dynamics using classical force fields, where the accuracy of predictions depends on the quality of the fitted force fields [55,71,72]. Other solvent-specific errors associated with continuum solvation techniques have

also been discussed [51].

In this work, we will only consider type 1 and type 2 solvation. In most cases, one explicit solvent molecule is included. This is reasonable because only one solvent molecule can covalently bond to the boron site. Solvent binding causes extensive geometric changes in most ABAs (Figure 42). In the ABA literature, to our knowledge, type 1 solvation has been used exclusively [40]. Even such a *purely* continuum approach (type 1) has predicted that the solvent reduces the differential affinity for F^- ($\Delta\Delta G_{F^-}$) among different ABA's, defined as the ΔG_{F^-} change when switching from one ABA to another (Equation 4), by approximately 25% compared to gas phase $\Delta\Delta G_{F^-}$ [39]. However, type 1 solvation does not yield the correct geometry changes in ABA (Figure 42). The present work shows that including an explicit solvent molecule is crucial for strong anion receptors, and can lead to a large modification of F^--binding free energy.

VASP calculations – To compute the zero temperature total energy of LiF solid, we apply the VASP code [73,74], PAW pseudopotentials [75], and PBE0 functional [57] in plane-wave-based DFT calculations carried out in periodic boundary conditions. The commonly used hybrid PBE0 functional is chosen because it is implemented in both G09 and in VASP. An energy cutoff of 500 eV for plane waves and a 10^{-5} eV wavefunction convergence criterion are enforced. The optimal lattice constant (4.02 Å) and cohesive energies are calculated in a face-centered cubic cell with a 2-atom unit cell and 4 × 4 × 4 Monkhorst-Pack Brillouin sampling. LiF phonon dispersions are then computed to estimate finite temperature corrections in the harmonic approximation. Phonon calculations apply the same settings, except that a 512-atom (16.08 Å)^3 supercell with Γ-point sampling is applied and the less expensive PBE functional is used for this larger simulation cell [76]. A finite difference approach is applied to calculate vibrational force constants. This yields the dynamical matrix, the eigenvalues of which are vibrational frequencies (ω) [77]. The vibrational correction to the free energy is:

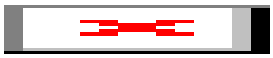

(12)

where β is the inverse thermal energy ($1/k_BT$), $\hbar$ is Planck's constant, {**k**} spans the Brillouin zone, and i is the composite index for the 6 eigenvalues ω_{ki} of the dynamical matrix at each **k**-point. Equation 12 yields a small, 0.067 eV thermal contribution. Therefore, we have not pursued improvement to the phonon calculation, e.g., via using the more accurate hybrid PBE0 functional.

Experimental method – Anion binding agents were synthesized using previously reported methods [78] and tested for electrochemical performance. The anion receptors considered include ABAO (IUPAC name: 2-(perfluorophenyl)-1,3,2-dioxaborolane-4,6-dione), ABAM (IUPAC name: 2-(perfluorophenyl)-1,3,2-dioxaborinane-4,6-dione), and a pinacol-based ABA (IUPAC name: 4,4,5,5-tetramethyl-2-(perfluorophenyl)-1,3,2- dioxaborolane) equivalent to ABA15 considered in Reference [46]. One additional step was executed to remove DMSO, used in synthesis, from the resulting products. All solids were re-dissolved in acetone with an excess of LiF. Undissolved LiF was removed by syringe filtration (2 μm) and the filtrate condensed by slow evaporation in air.

Electrochemical cells were assembled using 2032 coin cells, which utilized stainless steel electrodes separated with a polyimide spacer to ensure a uniform electrode separation. Electrolytes were composed of 3:7 (wt%) ethylene carbonate/ethyl methyl carbonate (EC:EMC) and 1.0 M ABA. Equivalents of 1.0 M LiF crystals were added to each electrolyte solution. All solutions were stirred thoroughly, but the total LiF content in solution was variable based upon the efficiency of fluoride binding by the ABA molecules. Lower affinity binding agents resulted in solutions that were much lower concentration than 1 M after filtration. Approximately 1 mL of electrolyte for each of the tested binding agents was flooded into the coin cell prior to sealing the cell shut. This was done to ensure that there was complete flooding of the electrochemically accessible area for both electrodes. Conductivity was determined using a Solartron 1287 and 1260 stack by measuring the AC impedance in the frequency range of 100 kHz to 0.1 Hz. The peak-to-peak voltage of the AC signal was limited to 5 mV to avoid any distortion in the response.

X-ray single-crystal data collection was conducted using a Bruker APEX/CCD diffractometer (Mo Kα, $\lambda = 0.71073$ Å). Indexing and frame integration were performed using the APEX-II software suite. Absorption correction was performed using SADABS (numerical method) also within the APEX-II software. The structures were solved and refined using SHELXS-97 contained in SHELXTL v6.10 packages.

4.1.2. Results for theoretical studies of boron-based anion receptors

Oxalate and boron ester ABA's are good anion receptors – Table 2 lists new predictions for ABAO, ABAT, and re-examines several fluoride receptors explored in Reference [46]. First we discuss their F^--binding free energies either in vacuum ($\varepsilon_0 = 1$), or with type 1 solvation using a polarizable dielectric continuum (PCM) implicit solvent model (Equation 8). The gas phase binding *enthalpy* (not shown) are comparable to those reported in Reference [45], although a somewhat different basis set is used compared with that work so as to be compatible with methods used for ABAO and ABAT herein. For a first estimation of solvation effects, ε_o is set to 40 to mimic a generic high dielectric liquid environment. As discussed above, for the purpose of this calculation, F^- is not solvated, and its energetic contribution is constant for all ABAs and solvents.

In vacuum (first row of Table 2), ABAO binds more strongly to F^- than almost all other ABA *X*'s, even those with multiple -C_6F_5 electron-withdrawing groups. The exception is ABAT, which is by far the most fluorophilic. As discussed in the introduction, ABAT alone has its boron atom in a non-planar geometry in its F^-−free state and is less adversely affected by the reorganization energy cost when binding F^-. When *only* the solvent dielectric continuum is added (second row of Table 2), the ΔG_{F^-} ordering remains largely unchanged. It is of interest to compare ABA12 and ABA15, which differ only by their -CF_3 and -CH_3 groups. The electron-withdrawing -CF_3 groups stabilize the F^- binding by 0.884 eV (20.4 kcal/mol) over ABA15.

Table 2 – F^- and CH_3CN ("S") binding free energies with various ABAs computed using Equations 7–9, in units of eV (~96 kJ/mol). No explicit solvent is present except in the last two rows (ABA-S and ABA-F^{-*}), where one CH_3CN is coordinated to the ABA boron site and Equation 9 (instead of Equation 8) is used to compute F^- binding free energy. ABA12 and ABA15 fail to bind to CH_3CN in the calculations.

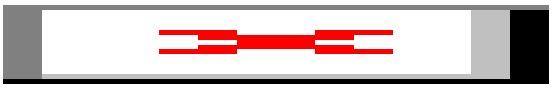

Including explicit CH_3CN solvent molecule(s) – Free energies computed using Equation 8 may overestimate F^--binding in polar solvents because the boron site may bond to solvent molecules. Next we examine the effect of an explicit CH_3CN solvent molecule coordinated to these ABA's (last two rows of Table 2). Figure 42 A, B, C depict the optimized, most enthalpically favorable geometries of ABA-CH_3CN at $\varepsilon_o = 40.0$. The N-atom terminus of the solvent coordinates to the boron site, just like F^- (Figure 41), leading to sp^3-hybridization of the B- atom and significant distortion of the molecular geometries compared with unbound ones (Figure 39A and Figure 39B). Such distortions are not observed when type 1 solvation treatment is used.

The solvent coordination reactions, ABAO+$CH_3CN \Leftrightarrow$ABAO-CH_3CN and ABAM+$CN_3CN \Leftrightarrow$ABAM-CH_3CN, exhibit free energy changes of −0.249 eV and −0.002 eV, respectively. CH_3CN binding to ABAO is therefore exothermic while it is almost thermoneutral for ABAM. Note that the zero temperature binding *enthalpies* to CH_3CN are favorable in both cases: −0.642 eV and −0.417 eV for ABAO and ABAM, respectively. As is typical of A + B ⇔ C reactions, the translational and rotational entropy penalties add up to more than 0.4 eV. They negate, or almost negate, the substantial favorable reaction enthalpies. ABAE and ABA21 also exhibit small CH_3CN binding free energies.

Since ABAO binds favorably to CH_3CN, Equation 9 should be used to examine F^- binding affinity. With the explicit solvent contribution added, the F^--affinity (ΔG_{F^-}) of ABAO lessens from −5.965 eV to −5.714 eV. For ABAM, ΔG_{F^-} is almost unmodified, becoming −5.648 eV (Table 2). Inclusion of explicit solvent therefore reduces the differential F^- affinity ($\Delta\Delta G_{F^-}$) between ABAO and ABAM from ~0.31 eV to ~0.07 eV. Even so, ABAO remains a slightly better F^- receptor. The F^--binding affinity of ABAE and ABA21 are slightly reduced when an explicit CH_3CN is included in the calculations. ABA12 and ABA15 do not bind to CH_3CN: even metastable ABA12-CH_3CN and ABA15-CH_3CN structures cannot be optimized with $\varepsilon_o = 40$ in the calculations. Hence Equation 8 should be used instead and their ΔG_{F^-} remains unchanged; and explicit CH_3CN should not be present in these models.

ABAT binds strongly to acetonitrile. The free energy associated with Equation 7 is −1.533 eV (−35 kcal/mol). If an explicit CH_3CN is not used in the calculations, the F^--binding affinity would be overestimated by this amount. This translates into a 6×10^{24} fold error in the equilibrium dissolution constant (K_{diss}, Equation 5). Subtracting Equation 7 from Equation 8 yields Equation 9, from which ΔG_{F^-} drastically drops from −7.238 eV to −5.705 eV. With this

significant modification due to explicit solvent effects, the F^- binding affinities of ABAO and ABAT in CH_3CN become almost identical, despite the large gas phase disparity.

We have also considered adding more solvent molecules to evaluate Equation 8. Figure 42g depicts six CH_3CN in the first solvation shell of ABAO, in addition to the use of the PCM dielectric surrounding the explicit solvent region. The F^- binding *enthalpies*, without vibrational corrections, are predicted to be −5.620 eV and −5.570 eV with one and six CH_3CN, respectively. They are within 50 meV of each other. When thermal and zero-point corrections are included, a slightly larger 80 meV difference is predicted. This is likely because the additional CH_3CN are only weakly coordinated to the ABAO- CH_3CN complex, yet the ABA-solvent interactions are still treated as harmonic vibrational modes. This approximation can lead to overestimated zero-point energy corrections that do not completely cancel in the reactants and products. Nevertheless, the predictions are sufficiently similar with 1 and 6 solvent molecules that we only consider one explicit molecule in all following calculations.

Survey of other solvent molecules, with ABAO, ABAM, and ABAT – DMSO is used during our synthesis of ABAO, and it exhibits the highest ABA-binding free energies among solvents examined in this work (Table 3). Figure 43 (left) depicts the X-ray crystal structure of ABAO-DMSO prior to solvent exchange, and after DMSO is replaced by F^-. The before-exchange (left panel) reconstruction clearly demonstrates that the boron site becomes sp^3 hybridized due to formation of a covalent bond with the oxygen site of DMSO. This hybridization remains after F^- substitutes for DMSO. There are also some extra materials not expected for this reconstruction post DMSO solvent-exchange (right panel). This is due to residual material that remains within the crystal structure during the evaluation. The software assigns lithium to the residual electron density remaining within the sample. The X-ray reconstruction in Figure 43 is sufficient to demonstrate the definitive change from DMSO-boron interaction to fluorine-boron interaction when an aggressive solvent exchange is conducted. Without this exchange, the primary reaction site for these ABA would be bound to solvents and unavailable for use to scavenge LiF during battery operation.

Table 3 – F^-- (ABA-F) and solvent-binding (ABA-S) free energies, Li^+ solvation free energies computed with an explicit solvent shell of 4 molecules ($Li^+ S_4$), and sum of these two (ABA-F/Li^+), in eV units (~96 kJ/mol). In the case of F^-, the asterisk refers to the corrected binding free energies (Equation 9) if the ABA binds to the solvent molecule (i.e., Equation 8 yields an attractive free energy). The ABA15-F/Li^+ value in EC solvent (ε_o = 40) is −8.926 eV. The *cis- trans* DMC conformation is most favorable when bound to ABA's.

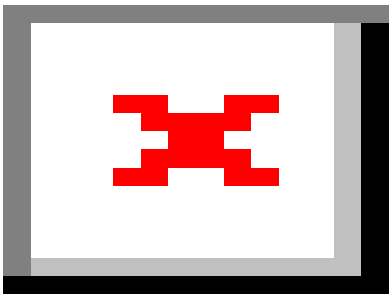

The DMSO-bound ABAO structure predicted from DFT (Figure 42e) looks similar to the left panel of Figure 43, except that the DMSO molecule is rotated so that one of its -CH_3 protons coordinates to an F^- on the phenyl ring. Since the calculation only contains one ABAO- DMSO complex, and omits explicit representation of the surrounding molecules to which DMSO can coordinate in the X-ray spectrum sample, the difference is understandable. The rotational conformational difference is not expected to lead to a significant change in the predicted energy.

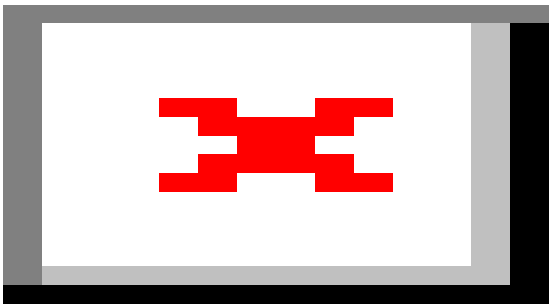

Figure 43. X-ray crystal structures of ABAO-DMSO prior to solvent exchange (left panel) and ABAO-F^- after solvent exchange (right panel). The color scheme used is slightly different from Figure 41 and Figure 42. F, B, and Li are in green, light pink, and dark pink instead of purple, dark green, and dark blue. Protons are subsumed into carbon atoms.

Table 3 shows that, at room temperature, both ABAO-DMSO and ABAM-DMSO complexes are favorable. Even after subtracting the free energy cost of breaking the ABA-DMSO bond to form ABA-F (i.e., using Equation 9 rather than Equation 8), ABAO retains a slight preference for F^--binding relative to ABAM in DMSO, while ABAT is slightly inferior to ABAO by ~0.1 eV.

Other solvents like DMC and EC have smaller specific solvent effects than DMSO (Table 3). EC exhibits an unfavorable binding free energy with ABAM. Therefore ABAM should retain its planar geometry, and type 1 dielectric continuum (Equation 10) calculations suffice for this ABA. In contrast, ABAO binds to all solvents. So does ABAT, which exhibits much larger binding free energies than ABAO. After subtracting the solvent-coordination effects, ABAT is predicted to be only slightly inferior to ABAO for binding-F^-.

LiF ionization and Li^+ solvation free energies – Using the VASP code, the free energy of splitting LiF solid into Li^+ and F^- ions in the gas phase (ΔG_{LiF}, Equation 2) is found to be 10.098 eV per formula unit. This includes finite temperature corrections due to solid state vibrational motion at $T = 300$ K (Equation 12) and the translational entropy gained by Li^+ and F^- corrected to 1.0 M concentration, even though the ions are assumed to be in gas phase in calculations associated with Equation 2. Gas phase entropic contributions cancel in the final results. Li^+ solvation free energies are also needed in dissolution predictions. With Li^+S_4 clusters and the PCM dielectric continuum approximation outside the cluster, Li^+ solvation free energies ($\Delta G_{solv-Li^+}$, Equation 3) in CH_3CN, DMSO, DMC, and EC are predicted to be −4.746 eV, −5.008 eV, −2.195 eV, and −4.445 eV, respectively, when computed at the respective ε_o of the pure solvent (Table 3). The EC result is consistent with earlier predictions of gas phase energy changes for LiF splitting and Li solvation [81]. Note that the DMC solvation value may be underestimated by a small fraction of an electronvolt due to the neglect of the significant

quadrupolar solvent contributions in the PCM dielectric continuum treatment, which is specific to this molecule [51, 82]. However, F^--binding to ABA in DMC is so much less favorable than in other solvents (Table 3) that this small solvation error should not affect the qualitative conclusions below.

LiF solubility predictions – The dissolution free energies (ΔG_{diss}) according to Equation 10 or 11 can now be calculated by adding ΔG_{F^-}, $\Delta G_{solv-Li^+}$ (the last rows of Table 3), and $\Delta G_{LiF} = 10.098$ eV. A negative ΔG_{diss} means that LiF dissolution is thermodynamically favorable. From Table 3, we predict that LiF should be mostly soluble in 1.0 M ABAO, ABAM, and ABAT in the presence of CH_3CN, DMSO, and EC. The exceptions are ABAM in EC and ABAT in EC and DMSO, where the solubility estimates are within the margin of computational uncertainties. Even though we have not applied the most advanced DFT functionals [81,83], the uncertainty of the computational method is unlikely to exceed a few tenths of an eV, while $\Delta\Delta G_{diss}$'s between different ABA's should be much more reliable than that.

As discussed in References [71] and [72], it is challenging to relate the predicted dissolution enthalpy (or free energy) to absolute solubility. Here the solubility for a binary compound like LiF is estimated via $(K_{diss})^{0.5}$ (Equation 6). We focus on EC molecules because they are the closest approximation to the electrolyte used in our experiments (an EC/EMC mixture) among the solvents examined in our modeling work. For ABAO-F^-/EC, Equation 11 yields $K_{diss} = \exp(-(-10.293 + 10.098)\text{ eV}/ k_B T)$. This translates into a 43.3 M solubility. The value is unphysically high because the calculations assume infinite Li^+ and ABAO-F^- dilution (i.e., ideal solution with unit solute activity) and neglect steric and electrostatic repulsion between like-charged ions. Inherent approximations in DFT functionals may also contribute to the extremely high value.

Nevertheless, the prediction of high LiF solubility in ABAO is consistent with the measured high mobility (Figure 44 below). With ABAM-F^-, the solubility is predicted to be a much lower 0.94 M. This value may again be overestimated. However, the trend that LiF solubility decreases going from ABAO to ABAM is qualitatively consistent with the reduced ABAM conductivity. We have also considered LiF solubility in ABA15 (not listed in Table 3). $\Delta G_{solv-Li^+}$ and ΔG_{F^-} sum to −8.966 eV in the presence of ABA15 with the EC-appropriate $\varepsilon_o = 40$ for type 1 solvation. The ABA15-assisted Li^+/F^- solubility in EC is predicted to be 1.5×10^{-10} M. Hence ABA15 is not expected to contribute to dissolution of LiF solid. The measured LiF solubility and conductivity in ABA15 may in fact reflect properties in the absence of any ABA.

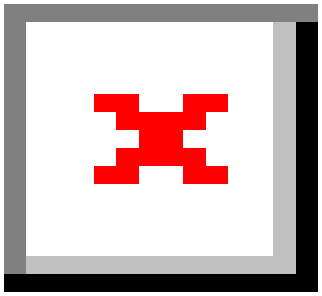

Figure 44. Electrolyte conductivity. Black, blue, and red represent 1.0 M ABAO, ABAM, and ABA15 added to the electrolyte (30:70 weight % EC/DMC), respectively.

LiF solubility in the absence of ABA is therefore needed for comparison purposes. Here we find that, if we treat Li^+ and F^- as well-separated solvated species surrounded by a dielectric continuum, the predicted solubility is a miniscule, unphysical 10^{-16}. This indirectly suggests that Li^+ and F^- must form ionic aggregates. We consider the two smallest charge-neutral aggregates, a Li^+/F^- contact ion pair (Figure 42h) and a Li_2F_2 cluster (Figure 42i). Three (3) and four (4) EC molecules are added to these clusters, respectively, to keep all Li^+ 4-coordinated to either EC or F^-. The LiF dissolution reactions in the absence of ABAs can be written as the respective cycles:

 (13)

 (14)

and

 (15)

 (16)

Solid state sublimation energies and liquid state solvation free energies are computed using the VASP and G09 codes. The resulting ΔG_{diss} for formation of a LiF contact ion pair is predicted to be +0.986 eV, which translates into a 5.3×10^{-9} M effective LiF solubility. This ion-pair solubility value is already larger than that computed for Li^+ and F^- solvation via formation of ABA15-F^- complexes. For Li_2F_2, ΔG_{diss} is +1.444 eV, which yields a 8.7×10^{-7} M solubility when $(K_{diss})^{0.25}$ is used to represent [Li^+] and [F^-] solubility. This is orders of magnitude higher than the contact ion pair value. The overall trend suggests that ion aggregates may be

responsible for much of the LiF solubility in the absence of ABAs. We will return to this point in the next subsection.

Using molecular dynamics simulations based on classical force fields, Tasaki *et al.* also predicted unfavorable heats of solvation for LiF solid in DMC and EC solvents in the absence of ABAs [71,72]. A direct comparison between these predictions and our results is difficult because different reference states are used. Unlike Li^+ and F^-, bulky ABA molecules are not likely to form aggregates, except for the constrained boron ester ABAT [44].

Conductivity measurements, experimental estimates of solubility, and comparison to DFT modeling – Figure 44 depicts the electrolyte conductivity measured in the coin cells as a function of temperature. ABAO exhibits the highest conductivity at all temperatures, while ABAM is a factor of 2-3 lower. The conductivity in ABA15 is negligible. Electrolyte conductivity should be strongly correlated with the ability of the electrolyte to dissolve LiF. The observed conductivity trend is therefore qualitatively consistent with the predicted ABAO>ABAM>ABA15 LiF solubility discussed in the last section.

To make a semi-quantitative estimate of the amount of lithium in solution when ABA15 is present, it was assumed that the conductivity varied with concentration, similar to other battery electrolyte systems [79, 80]. The conductivity of the ABAO solutions was assumed to be maximized for the purpose of this analysis (i.e., all LiF added was dissolved, yielding a 1.0 M concentration). Also, ABAO was used as a reference for the ABA15 solution. Conductivities were then approximated using a fourth order polynomial fit [79]. The concentration of dissolved LiF that was calculated in solution using this evaluation for the ABA15 solution was approximately 5×10^{-4} mol/L. This represents a large reduction in overall fluoride binding affinity for ABA15 over the other demonstrated binding agents. As mentioned above, our estimated 5×10^{-4} mol/L LiF solubility in the ABA15 solution is likely due to Li^+ and F^- ions and their ionic aggregates, and not due to ABA15-F^- complexation.

Tasaki et al. reported that the LiF concentration in neat DMC is $1.7 \pm 0.4 \times 10^{-4}$ mol/L, or 4±1 ppm after filtration through 2 μm filter [71]. This is slightly lower but is of the same order of magnitude as the 5×10^{-4} mol/L solubility we estimate for EC/EMC/apparently-inert ABA15. EC/DMC has a higher dielectric constant and is expected to be a better solvent for LiF dissolution. Hence their measurements and ours are broadly consistent with each other.

Jones et al. have shown that LiF solubility in the absence of ABAs can strongly depend on whether filtration was performed, and on the filtering pore sizes [84]. Without filtering, LiF solubility in DMC was reported at 2.2×10^{-2} mol/L [84], more than 100 times higher than post-filtering [71]. Large pore sizes in filtering crucible also increase the apparent LiF solubility [84]. The solubility of LiF in EC or EC mixtures was only reported without filtering, and a direct comparison with filtered DMC/LiF solutions cannot be made.

The study of Jones et al. appears to confirm the role of LiF ionic aggregates in LiF solubility suggested by our calculations [84]. As discussed above, LiF solubility increases as the end product varies from isolated Li^+ and F^-, to LiF pairs, to Li_2F_2 clusters, although there remains a substantial difference between the cluster sizes considered in theory and experimental pore sizes.

Quantitatively, the DFT-predicted LiF solubility of 8.7×10^{-7} M remains substantially below the experimental estimate of $\sim 5 \times 10^{-4}$ M. However, the discrepancy is expected to shrink as larger clusters are considered in DFT calculations. In the future, it is of interest to estimate the LiF solubility in the absence of ABA using nanofiltration-prepared electrolytes in experiments, and at the same time perform simulations of higher order aggregates $(LiF)_n$, $n > 2$, which are more costly computationally, to further confirm this point.

4.1.3. Conclusions for theoretical studies of boron-based anion receptors

Using both DFT predictions and conductivity measurements, we have shown that the oxalate-based ABA ("ABAO") has LiF-solvation properties that make it a promising fluoride receptor for primary carbon monofluoride (CFx) batteries. The suitability of this anion receptor in other batteries like lithium-ion or lithium-air may depend on factors other than LiF conductivity [45], such as its interaction with PF^-_6, which is not present in primary batteries. However, the solvent effects emphasized in this work have general interest in liquid electrolyte-based energy storage devices beyond CFx.

After accounting for explicit solvent effects, the equilibrium constant K_{diss} for the reaction with ABAO:

(17)

is the largest among the ABAs tested here. The trend is confirmed by explicitly comparing the conductivity of three ABAs we have synthesized and tested. The predicted LiF solubility in ABAO is at least comparable to that of a recently proposed ABAT with the boron atom in a non-planar environment [44], after specific solvent effects are taken into account. Indeed, for these strong F^-–binding anion receptors, we find that including explicit ABA-S covalent bonding for different choices of solvent is crucial. Omitting the solvent molecule in the calculations can lead to ABA-F^- binding coefficients that are in error by many orders of magnitude. Our results therefore emphasize the importance of considering explicit F^- and solvent-molecule binding in calculations when conducting computational design/screening of an- ion receptors. In the absence of ABAs, we propose that LiF dissolves in cyclic carbonate organic solvents mostly through the formation of ionic aggregates; isolated and well-solvated Li^+ and F^- species likely exist at low concentrations in LiF solutions.

4.2. Dielectric Properties of Ethylene and Propylene Carbonate using Molecular Dynamics Simulations

4.2.1. Introduction

Since batteries operate at a range of temperatures, the variation in electrolyte properties with temperature is an important consideration in electrolyte development. Experimental and simulation studies of the dielectric properties of pure EC and PC solvents (Figure 45) at wide ranges of temperature are limited [85-90]. Here, we address the dielectric constant and dielectric relaxation times for pure EC and PC electrolytes at temperatures ranging from room temperature (300 °K) to 600 °K. Specifically, we carry out molecular simulation studies with all-atom force

fields and compare the computed dielectric properties against available experimental results to test the force fields.

Dipole relaxation processes provide insight about solvent dynamical properties. The molecular polarization in a dielectric medium does not respond instantly to a changing electric field. The delay depends on the frequency of the changing electric field. At low frequency, the polarization nearly achieves its equilibrium value because the dipoles can satisfactorily reorient to the changing field. At high frequency, the dipole reorientation lags behind the field [91]. Dielectric relaxation assesses the lag of the material polarization in responding to a change in an applied electric field.

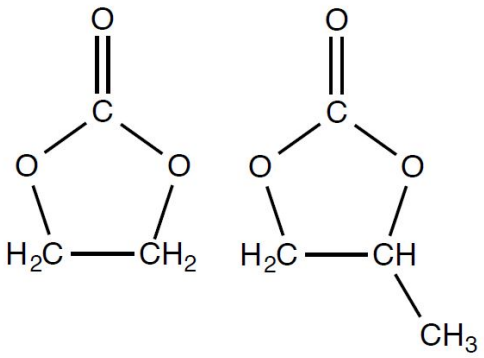

Figure 45. Chemical structures of ethylene carbonate (EC) and propylene carbonate (PC).

The frequency-dependent dielectric constant can be written as, [91-93]

$$\epsilon(\omega) = \epsilon'(\omega) - i\epsilon''(\omega). \tag{18}$$

The imaginary part, ϵ''(ω), is the dielectric loss and describes energy lost as heat. In terms of the cosine transform of the dipole moment autocorrelation function,

$$P(t) = \frac{\langle M(0)M(t)\rangle - \langle M(0)\rangle^2}{\langle M(0)^2\rangle - \langle M(0)\rangle^2}\ , \tag{19}$$

ϵ''(ω) is given by [86, 93, 94]

$$\frac{\epsilon''(\omega)}{\epsilon\,(\omega=0) - \epsilon_0} = \omega \int_0^\infty P(t)\cos(\omega t)\,\mathrm{d}t\ . \tag{20}$$

Here M(t) is the dipole moment of the simulated system at time t, ϵ_0 is the permittivity of free space, and the relative electric permittivity $\epsilon(\omega=0)/\epsilon_0$ is the static dielectric constant. This formula (Equation 20) explicitly recognizes the absence of electronic polarization in the present

simulation model, and thus sets the traditional infinite frequency relative permittivity to unity; $\epsilon(\omega=\infty)/\epsilon_0 = 1$.

We fit the computed P(t) to a Kohlrausch-Williams-Watts (KWW) model,

$$P_{\mathrm{KWW}}(t) = \exp[-(t/\tau)^{\beta}] \ . \tag{21}$$

This model accounts for symmetric and asymmetric broadening of the dielectric loss. The temperature dependence of the relaxation time may be modeled as

$$\tau^{-1} = A \exp\left(-H^*/k_{\mathrm{B}}T\right) \ , \tag{22}$$

with H^* an activation enthalpy that we assume here to be independent of T. Furthermore, though specific forms of the pre-exponential factor A are debated [86, 95, 96], we consider that factor a constant parameter for these results. Then H^* can be evaluated from the 1=T slope of the Arrhenius plot

$$\ln \tau \propto H^*/k_{\mathrm{B}}T \ . \tag{22}$$

Finally, with Equation 21 we implemented the cosine transform Equation 20 [94] to examine $\epsilon''(\omega)$ using the Cole-Cole plot.

4.2.2. Methods

Molecular dynamics simulations were carried out using the Gromacs simulation package [97]. Solvent molecules (249 EC and 1000 PC) were placed randomly in a cubic simulation box (end length 3 nm and 6 nm) to generate initial configurations. The OPLS-AA force field parameters were used to represent both EC and PC molecules [98]. Periodic boundary conditions were applied to mimic bulk liquid conditions. An energy minimization calculation and 1 ns of density equilibration were followed by a 50 ns production run using a constant pressure ensemble (NPT). Configurations were sampled every 2 ps for the dielectric constant calculations. A Nose-Hoover thermostat [99, 100] maintained the temperature, and the Parrinello-Rahman barostat [101] set the pressure at 1 atm throughout the simulation. Bonds involving hydrogen atoms were constrained using the LINCS algorithm [102]. The particle mesh Ewald method with cut-off at 1.2 nm was used to compute electrostatic interactions.

A separate 1 ns simulation was run to calculate the dipole autocorrelation function, P(t). Configurations were saved at every 0.001 ps to achieve satisfactory time resolution. Other simulation conditions were the same as above.

4.2.3. Results

The static dielectric constants ϵ/ϵ_0 of PC and EC at various temperatures are shown in Figure 46. These graphs clearly show that the fluctuations at the beginning of the simulation are large. Thus, the system must be equilibrated long enough to obtain a reasonable value for the average static dielectric constant. The high viscosity and large permanent dipole moment of the electrolytes are responsible for the slow convergence of average dielectric constant. At higher

temperature, both the viscosity and dipole moment decrease, thereby decreasing the time for convergence. The mean absolute values of the dipole moment and dielectric constant are given in Table 2. The dipole moments are larger than the experimental values due to lack of polarization in the OPLS-AA model.

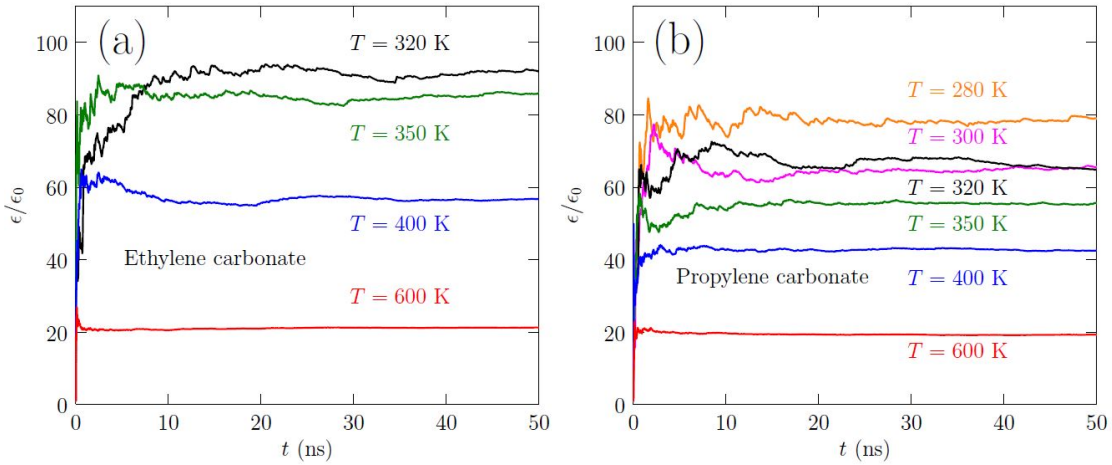

Figure 46. Static dielectric constant of PC and EC as a function of simulation time at various temperatures.

The static dielectric constants calculated from the simulation trajectories for pure EC and PC solutions [Table 2] agree satisfactorily with the available experimental results (Figure 47a). For example, experimental results are $\epsilon/\epsilon_0 = 89$ and 64 for EC (320 °K) and PC (300 °K), respectively, and the computed values are 92.3 and 66.2 for the same cases [86].

Table 4 – Static dielectric constant ϵ/ϵ_0, dipole moment μ, relaxation time τ, and stretch parameter β of EC and PC as a function of temperature. See Equation 21. Note that the stretch parameter β is distinctly less than one.

	T (K)	ϵ/ϵ_0	μ (Debye)	τ	β
EC	320	92.3	5.54±0.11	18.5	0.84
	350	86.2	5.47±0.15	11.9	0.83
	400	56.9	5.46±0.16	7.0	0.86
	600	21.4	5.43±0.2	1.9	0.92
PC	280	78.4	6.47±0.15	78.9	0.84
	300	66.2	6.47±0.15	47.5	0.84
	320	63.2	6.46±0.16	30.1	0.89
	350	55.8	6.46±0.16	19.2	0.86
	400	42.2	6.45±0.17	10.7	0.88
	600	19.2	6.42±0.21	2.7	0.92

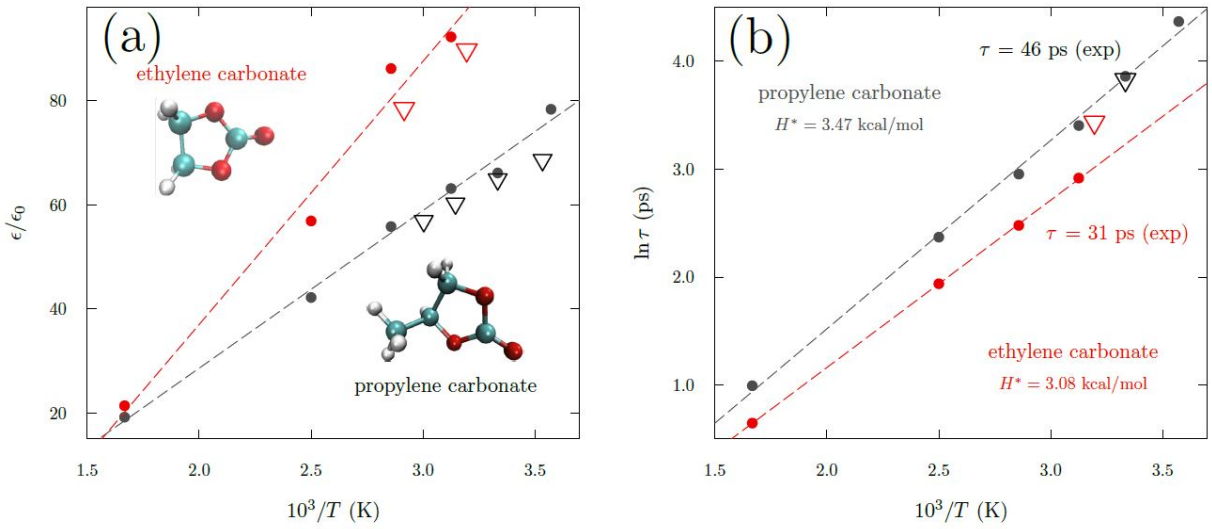

Figure 47. (a) Static dielectric constants ϵ/ϵ_0, and (b) relaxation times τ of EC and PC at various temperatures. Experimental data is shown in open triangles.[93]

Dipole auto-correlation functions calculated for the simulation trajectory (Figure 48) are fitted to Equation 21. The stretch parameter β was always less than 1 and increased with the temperature.

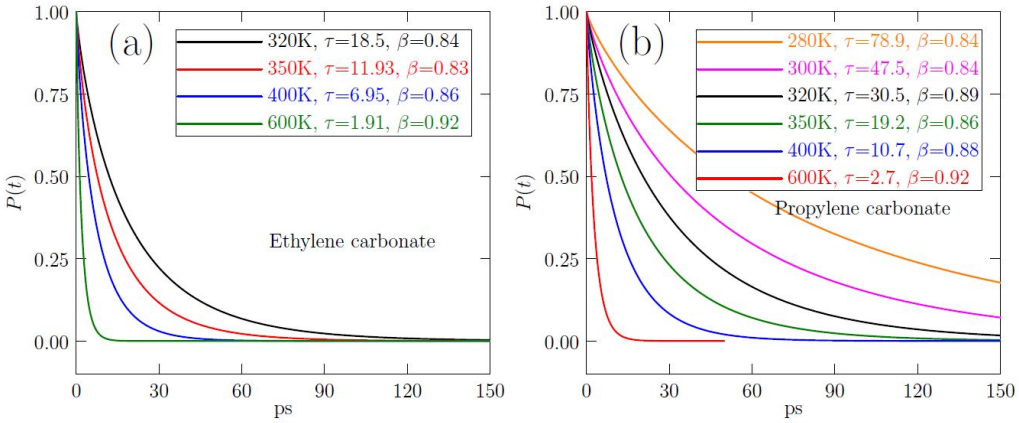

Figure 48. Dipole auto-correlation functions for (a) EC and (b) PC.

The dielectric relaxation times are remarkably long on a simulation time scale, even though these are small-molecule liquids. Still the agreement with experiment (Figure 47b) is encouraging: τ = 46 ps from experiment on PC at room temperature compared to τ = 47.5 ps from simulations. The extracted activation parameters H^* are 3.08 kcal/mol and 3.47 kcal/mol for EC and PC (Figure 47b). The Cole-Cole plot predicted a single relaxation process due to a semi-circular plot (Figure 49). Since the relaxation times naturally decrease with increasing temperature, the peak in $\epsilon''(\omega)$ (Figure 50) broadens and lowers with higher T and the radius of the semicircle in the Cole-Cole plot decreases (Figure 49). The comparison with relaxation times from experiment is again encouraging, though we note that the analysis of experiments requires assessment of factors, such as electronic polarizability $\epsilon(\omega=\infty)/\epsilon_0 = 0$, that we deliberately avoid here.

4.2.4. Dielectric Properties of Carbonates Conclusions

The OPLS-AA force field parameters for EC and PC provide reasonable agreement with the available experimental data on pure solvent dielectric properties, both for the static dielectric constant and the dielectric relaxation times. This study provides a benchmark for force field parameters for pure EC and PC solutions and can be extended to study the electrical properties of mixed electrolyte solutions.

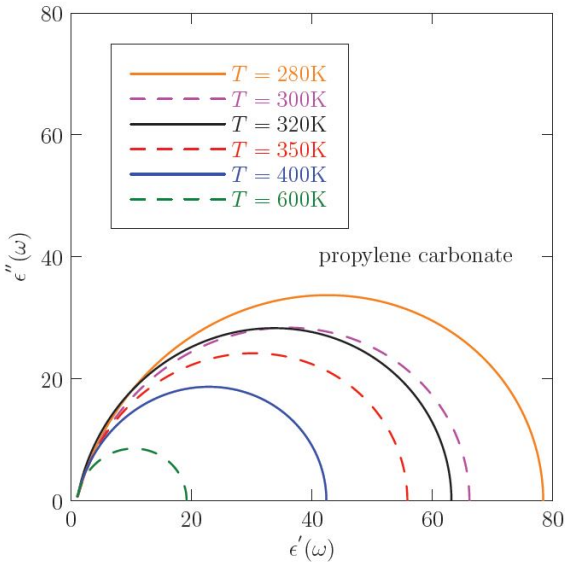

Figure 49. Cole-Cole plot for propylene carbonate at various temperatures.

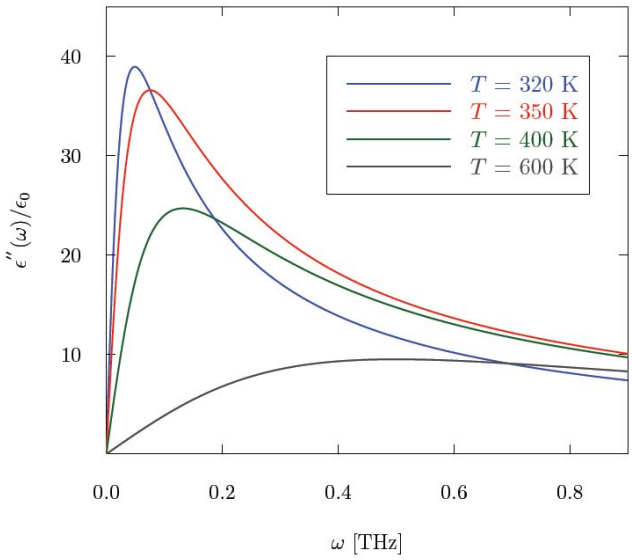

Figure 50. Frequency dependent dielectric loss for EC.

5. CONCLUSIONS

The need for new materials that can enable higher energy density power sources while utilizing non-flammable and non-toxic materials is becoming a universal necessity for almost every industry. The push towards increasingly complex systems with ever increasing demands for capacity will ensure that these pressures on battery research will not disappear any time soon. There are few options with regards to lithium primary systems that offer opportunity for dramatic growth. Investigation into new materials for the carbon monofluoride system offers an opportunity for increasing primary battery safety while offering potential electrochemical performance increases.

By synthesizing and characterizing completely new solvents that offer promise for increasing battery performance, there are opportunities for dramatic improvement in battery capacity, rate performance, and safety. The materials and evaluations described previously offer several improvements and several deficiencies for battery performance in several areas. Several of the previously un-synthesized materials also have potential in other applications outside of lithium primary batteries. Much of the knowledge gained in this program will hopefully be impactful towards future work. Development of new materials with potential new mechanisms and properties will be key to the expansion of battery performance. Without a large increase in battery performance through materials discoveries or new electrochemical systems, it is likely that technology may vastly outpace the ability for the electrochemical power sources to provide reliable and safe power.

6. REFERENCES

[1] N.A.A. Rossi and R. West, "Silicon-containing liquid polymer electrolytes for application in lithium ion batteries," *Polym. Int.*, **2009**, *58*, 267–272.

[2] L. Zhang, Z. Zhang, S. Harring, M. Straughan, R. Butorac, Z. Chen, L. Lyons, K. Amine, and R. West, "Highly conductive trimethylsilyl oligo(ethylene oxide) electrolytes for energy storage applications," *J. Mater. Chem.*, **2008**, *18*, 3713–3717.

[3] Z. Zhang, L. Lyons, R. West, K. Amine, and R. West, "Synthesis and ionic conductivity of mixed substituted polysiloxanes with oligoethyleneoxy and cyclic carbonate substituents," *Silicon Chem.*, **2005**, *3*, 259–266.

[4] H.S. Lee, Y.Q. Yang, X. Sun, J. McBreen, "Synthesis of a new family of fluorinated boronate compounds as anion receptors and studies of their use as additives in lithium battery electrolytes," *J. Power Sources*, **2001**, 97-8, 566-569.

[5] X. Sun, H.S. Lee, X.Q. Yang, J. McBreen, "A new additive for lithium battery electrolytes based on alkyl borate compound," *J. Electrochem. Soc*, **2002**, 149, A355-A359.

[6] P. Lam and R. Yazami, "Physical characteristics and rate performance of $(CF_x)_n$ ($0.33<x<0.66$) in lithium batteries," *J. Power Sources*, **2006**, 153, 354-359.

[7] S. Zhang, D. Foster, J. Wolfenstine, J. Read, "Electrochemical characteristic and discharge mechanism of a primary Li/CF_x cell," *J. Power Sources*, **2009**, 187, 233-237.

[8] OSHA (PEL) – General Industry, Document 29 CFR 1910.1000 Table Z-1.

[9] J. Cabana, L. Monconduit, D. Larcher and M. R. Palacín, (2010) Adv. Mater. 22:E170–E192.

[10] D. Shanmukaraj, S.Grugeon, G. Gachot, S. Laruelle, D. Mathiron, J-M Tarascon, and Michel Armand (2010) J. Amer. Chem. Soc. 132:3055–3062.

[11] B. Xie, H.S. Lee, H. Li, X.Q. Yang, J. McBreen, L.Q. Chen (2008) Electrochemistry Communications 10:1195–1197.

[12] L.F. Li, B.Xie, H.S. Lee, H.Li, X.Q. Yang, J. McBreen, X.J. Huang (2009) Journal of Power Sources 189:539–542.

[13] G. Nagasubramanian, Kyle Fenton (2013) Electrochimica Acta 101:3-10.

[14] G. Nagasubramanian, C. Orendorff (2011) Journal of Power Sources 196:8604 -8609.

[15] G. Nagasubramanian, Bryan Sanchez (2007) Journal of Power Sources 165:630–634.

[16] H.F. Xiang, H.Y. Xu, Z.Z. Wang, C.H. Chen (2007) Journal of Power Sources 173:562-564.

[17] J.K. Feng, X.P. Ai, Y.L. Cao, H.X. Yang (2008) Journal of Power Sources 177:194-198.

[18] J. K. Feng, X.J. Sun, X.P. Ai, Y.L. Cao, H. X. Yang (2008) Journal of power Sources 184:570-573.

[19] M. Ue, Y. Sasaki, Y. Tanaka, and M. Morita (2014) in: T.R. Jow, K. Xu, O. Borodin, M. Ue Nonaqueous Electrolytes with Advances in Solvents Chpt. 2:Vol. 58:Pg. 476.

[20] X. Sun, H. S. Lee, X.-Q. Yang, and J. McBreen (2002) Electrochemical and Solid-State Letters 5:A248-A251.

[21] W. C. West, J. F. Whitacre, N. Leifer, S. Greenbaum, M. Smart, R. Bugga, M. Blanco, and S. R. Narayanan (2007) Journal of The Electrochemical Society 154:A929-A936.

[22] Zhang, L.; Zhang, Z.; Harring, S.; Straughan, M.; Butorac, R.; Chen, Z.; Lyons, L.; Amine, K.; West, R. "Highly conductive trimethylsilyl oligo(ethylene oxide) electrolytes for energy storage applications," *J. Mater. Chem.* **2008**, *18*, 3713.
[23] Zhang, Z.; Dong, J.; West, R.; Amine, K. "Oligo(ethylene glycol)-functionalized disiloxanes as electrolytes for lithium-ion batteries," *J. Power Sources* **2010**, *195*, 6062.
[24] Wen-Zheng, G.; Li-Qing, H.; Wei-Yuan, H. "The Nucleophilic reaction of polyfluoroaromatic compounds. II. Nucleophilic cyclization of chloropentafluorobenzene," *Chin. J. Chem.* **1988**, *6*, 238.
[25] *Comprehensive Handbook on Hydrosilylation*; 1st ed.; Marciniec, B., Ed.; Pergamon Press: New York, NY, 1992.
[26] *Boronic Acids: Preparation, Applications in Organic Synthesis and Medicine*; Hall, D. G., Ed.; Wiley-VCH: Weinheim, 2006.
[27] Ishiyama, T.; Murata, M.; Miyaura, N. "Palladium(0)-Catalyzed Cross-Coupling Reaction of Alkoxydiboron with Haloarenes- A Direct Procedure for Arylboronic Esters Ishiyama," *J. Org. Chem.* **1995**, *60*, 7508.
[28] Adamczyk-Woźniak, A.; Jakubczyk, M.; Jankowski, P.; Sporzyński, A.; Urbański, P. M. "Influence of the diol structure on the Lewis acidity of phenylboronates," *J. Phys. Org. Chem.* **2013**, *26*, 415.
[29] Greene, T. W.; Wuts, P. G. M. *Protective Groups in Organic Synthesis*; 3rd ed.; John Wiley & Sons: New York, NY, 1999.
[30] Beckett, M. A.; Rugen-Hankey, M. P.; Sukumar Varma, K. "Synthesis and characterisation of cyclo-boratetrasiloxane, (RBO)(Me2SiO)3 (R=nBu, Ar), derivatives," *Polyhedron* **2003**, *22*, 3333.
[31] H.F. Xiang, H.Y. Xu, Z.Z. Wang, C.H. Chen (2007) Journal of Power Sources 173:562-564.
[32] J.K. Feng, X.P. Ai, Y.L. Cao, H.X. Yang (2008) Journal of Power Sources 177:194-198.
[33] J. K. Feng, X.J. Sun, X.P. Ai, Y.L. Cao, H. X. Yang (2008) Journal of power Sources 184:570-573.
[34] G. Nagasubramanian, M. Rodriguez (2007) Journal of Power Sources 170:179–184.
[35] K. Xu (2004) Chemical Reviews 104:4303-4418.
[36] L.F. Li, H.S. Lee, H. Li, X.Q. Yang, and X.J. Huang (2009) Electrochemistry Communications 11:2296–2299.
[37] G. Nagasubramanian (2001) J. Applied Electrochemistry 31:99-104.
[38] S.S. Zhang, K. Xu, T.R. Jow (2003) J. Solid state Electrochem 7:147-151.
[39] K. Leung, M.I. Chaudhari, S.B. Rempe, K.R. Fenton, H.D. Pratt III, C.L. Staiger, G. Nagasubramanian. J. Electrochem. Soc., 162 (9) A1927-1934 (2015).
[40] V. P. Reddy, M. Blanco, and R. Bugga, J. Power Sources, 247, 813 (2014).
[41] X. Sun, H. S. Lee, S. Lee, X.-Q. Yang, and J. McBreen, Electrochem. Solid-State Lett., 1, 239 (1998).
[42] H. S. Lee, X. Q. Yang, C. L. Xiang, J. McBreen, and L. S. Choi, J. Electrochem. Soc., 145, 2813 (1998).
[43] N. G. Nair, M. Blanco, W. West, F. C. Weise, S. Greenbaum, and V. P. Reddy, J. Phys. Chem. A, 113, 5918 (2009).
[44] D. Shanmukaraj, S. Grugeon, G. Gachot, S. Laruelle, D. Mathiron, J.-M. Tarascon, and M. Armand, J. Am. Chem. Soc., 132, 3055 (2010).

[45] Y. Qin, Z. Chen, H. S. Lee, X.-Q. Yang, and K. Amine, J. Phys. Chem. C, 114, 15202 (2010).
[46] Z. Chen and K. Amine, J. Electrochem. Soc., 156, A672 (2009).
[47] L.F.Li, H.S.Lee, H.Li, X.-Q.Yang, and X.J.Huang, Electrochem.Commun.,11, 2296 (2009).
[48] Y. Zhu, Y. Li, and D. P. Abraham, J. Electrochem. Soc., 161, A1580 (2014).
[49] NS. Choi, S.W. Ryu, and J.K. Park, Electrochem. Acta, 53, 6575 (2008).
[50] E. Rangasamy, J. Li, G. Sahu, N. Dudney, and C. Liang, J. Am. Chem. Soc., 136, 6874 (2014).
[51] T. A. Barnes, J. W. Kaminski, O. Borodin, and T. F. Miller, J. Phys. Chem. C, 119, 3865 (2015).
[52] K. Leung, Chem. Phys. Lett., 568-569, 1 (2013).
[53] D. M. Rogers, D. Jiao, L. R. Pratt, and S. B. Rempe, in Annual Reports in Computational Chemistry, ed. R. A. Wheeler, Elsevier, New York, vol. 8, ch. 4. pp. 71 (2012).
[54] Moderate affinities between boron in anion receptors and tertiary amine groups on solvent molecules have been reported. See G. Go´mez-Jaimes and V. Barba, J. Mol. Structure, 1075, 594 (2014), and references therein.
[55] S. D. Han, O. Borodin, D. M. Seo, Z. B. Zhou, and W. A. Henderson, J. Electrochem. Soc., 161, A2042 (2014).
[56] K. Sodeyama, Y. Yamada, K. Aikawa, A. Yamada, and Y. Tateyama, J. Phys. Chem. C, 118, 14091 (2014).
[57] C. Adamoand, V. Barone. J. Chem. Phys.,110,6158(1999).
[58] Gaussian 09, Revision A.1, M. J. Fritsch et al., Gaussian, Inc., Wallingford CT, 2009.
[59] G. Scalmaniand, M.J. Frisch, J. Chem. Phys., 132, 114110(2010).
[60] S. Yanase and T. Oi, Journal of Nuc. Sci. Tech., 39, 1060(2002).
[61] Y.Wang and P.B.Balbuena, Int. J. Quant. Chem.,102, 724(2005).
[62] K. Leung and J. L. Budzien, Phys. Chem. Chem. Phys., 12, 6583 (2010).
[63] S.B. Rempe, L.R. Pratt,G. Hummer, J.D. Kress, R.L. Martin, and A.Redondo, J. Am. Chem. Soc., 122, 966 (2000).
[64] T. M. Alam, D. Hart, and S. B. Rempe, Phys. Chem. Chem. Phys., 13, 13629 (2011).
[65] P. E. Mason, S. Ansell, G. W. Neilson, and S. B. Rempe, J. Phys. Chem. B, 119, 2003 (2015).
[66] L.M. Menteland, E.J. Baerends. J. Chem. Theory Comput., 10, 252(2014).
[67] S.D. Han, O. Borodin, D.M. Seo, Z.B. Zhou, and W.A. Henderson. J. Electrochem. Soc., 161, A2042 (2014).
[68] S. B. Rempe and H. Jo¨nsson, The Chemical Educator, 3, 1 (1998).
[69] R. Car and M. Parrinello, Phys. Rev. Lett., 55, 2471(1985).
[70] V. S. Bryantsev, Theor. Chem. Acc., 131, 1250 (2010).
[71] K. Tasaki, A. Goldberg, J.-J. Lian, M. Walker, A. Timmons, and S. J. Harris, J. Electrochem. Soc., 156, A1019 (2009).
[72] K. Tasakiand, S.J. Harris. J. Phys. Chem.C, 114, 8076(2010).
[73] G. Kresseand, G. Furthmuller. Phys. Rev. B, 54, 11169(1996).
[74] J. Paier, M. Marsman, and G. Kresse, J. Chem. Phys., 127, 024103 (2007).
[75] G. Kresseand, J. Joubert. Phys.Rev.B, 59, 1758(1999).
[76] J.P. Perdew, K. Burke, and M. Ernzerhof. Phys. Rev. Lett., 77, 3865(1996).
[77] P. Giannozzi, S. de Gironcoli, P. Pavone, and S. Baroni. Phys.Rev.B, 43, 7231(1991).

[78] L. F. Li, B. Xie, H. S. Lee, H. Li, X.-Q. Yang, J. McBreen, and X. J. Huang, J Power Sources, 189, 539 (2009).
[79] M. S. Ding, K. Xu, S. S. Zhang, K. Amine, G. L. Henriksen, and T. R. Jow, J. Electrochem Soc., 148, A1196 (2001).
[80] J. P. Southall, H. V. S. A. Hubbard, S. F. Johnston, V. Rogers, G. R. Davies, J. E. McIntyre, and I. M. Ward, Solid State Ionics, 85, 51 (1996).
[81] E. Jonsson and P. Johansson, Phys. Chem. Chem. Phys., 14, 10774 (2012).
[82] N. Sai, R. Gearba, A. Dolocan, J. R. Tritsch, W.-L. Chan, J. R. Chelikowsky, K. Leung, and X. Zhu, J. Phys. Chem. Lett., 3, 2173 (2012), and references therein.
[83] O. Borodin and G. D. Smith, J. Phys. Chem. B, 113, 1763 (2009).
[84] J. Jones, M. Anouti, M. Caillon-Caravanier, P. Willmann, P.-Y. Sizaret, and D. Lemordant, Fluid Phase Equ., 305, 121 (2011).
[85] G. Pistoia, Lithium-Ion Batteries, ser. Advances and Applications. Newnes, Dec. 2013.
[86] R. Payne and I. E. Theodorou, J. Phys. Chem., vol. 76, pp. 2892-2900, Sep. 1972.
[87] X. You, M. I. Chaudhari, L. R. Pratt, and N. Pesika, J. Chem. Phys., vol. 138, p. 114708, 2013.
[88] L. Yang, B. H. Fishbine, A. Migliori, and L. R. Pratt, J. Chem. Phys., vol. 132, p. 044701, Jan. 2010.
[89] L. B. Silva and L. C. G. Freitas, J. Mol. Struc.: THEOCHEM, vol. 806, pp. 23-34, Mar. 2007.
[90] J.-C. Soetens, C. Millot, B. Maigret, and I. Bako, J. Mol. Liq., vol. 92, pp. 201-216, Jul. 2001.
[91] D. McQuarrie, Statistical Mechanics. University Science Books, 2000.
[92] C. P. Smyth, Dielectric behavior and structure; dielectric constant and loss, dipole moment and molecular structure. McGraw-Hill,-1955.
[93] G. Williams, Adv. Poly. Sci. Springer, 1979.
[94] O. Borodin, D. Bedrov, and G. D. Smith, Macromol., vol. 35, pp. 2410-2412, Feb. 2002.
[95] M. T. Hosamani, N. H. Ayachit, and D. K. Deshpande, J. Mol. Liq., vol. 137, pp. 43-45, Jan. 2008.
[96] L. Zhang and M. L. Greenfield, J. Chem. Phys., vol. 127, p. 194502, 2007.
[97] D. Van Der Spoel, E. Lindahl, B. Hess, G. Groenhof, A. E. Mark, and H. J. C. Berendsen, J. Comp. Chem., vol. 26, pp. 1701-1718, Dec. 2005.
[98] W. L. Jorgensen and D. S. Maxwell, J. Am. Chem. Soc., vol. 118, pp. 1657-1666, 1996.
[99] S. Nose, Mol. Phys., vol. 52, pp. 255-268, Aug. 1984. http://www.tandfonline.com/doi/abs/10.1080/00268978400101201
[100] W. G. Hoover, Phys. Rev. A, vol. 31, pp. 1695-1697, Mar. 1985.
[101] M. Parrinello and A. Rahman, J. App. Phys., vol. 52, pp. 7182-7190, 1981.
[102] B. Hess, H. Bekker, H. J. C. Berendsen, and J. G. E. M. Fraaije, J. Comp. Chem., vol. 18, pp. 1463-1472, 1997.

7. Distribution

1	MS0359	D. Chavez, LDRD Office	1911
1	MS0613	Harry Pratt	2546
1	MS0613	Travis Anderson	2546
1	MS0614	Trish Selcher	2545
1	MS0614	Kyle Fenton	2545
1	MS0614	Ganesan Nagasubramanian	2545
1	MS0734	Chad Staiger	6124
1	MS1315	Susan Rempe	8635
1	MS1315	Mangesh Chaudhari	8635
1	MS1415	Kevin Leung	1131
1	MS0899	Technical Library	9536 (electronic copy)


Sandia National Laboratories